



UNIVERSIDAD NACIONAL AUTÓNOMA DE MÉXICO
PROGRAMA DE MAESTRÍA Y DOCTORADO EN INGENIERÍA
INGENIERÍA CIVIL – ESTRUCTURAS

FORMULATION AND NUMERICAL IMPLEMENTATION OF AN IMPROVED
FINITE ELEMENT MODEL AND ITS APPLICATION TO THE STUDY OF
ANCIENT MASONRY STRUCTURES

TESIS
QUE PARA OPTAR POR EL GRADO DE:
MAESTRO EN INGENIERÍA

PRESENTA:
HÉCTOR RODRIGO AMEZCUA RIVERA

TUTOR PRINCIPAL
DR. A. GUSTAVO AYALA MILIÁN, INSTITUTO DE INGENIERÍA

CIUDAD UNIVERSITARIA, CDMX. 2016



Universidad Nacional
Autónoma de México



UNAM – Dirección General de Bibliotecas
Tesis Digitales
Restricciones de uso

DERECHOS RESERVADOS ©
PROHIBIDA SU REPRODUCCIÓN TOTAL O PARCIAL

Todo el material contenido en esta tesis esta protegido por la Ley Federal del Derecho de Autor (LFDA) de los Estados Unidos Mexicanos (México).

El uso de imágenes, fragmentos de videos, y demás material que sea objeto de protección de los derechos de autor, será exclusivamente para fines educativos e informativos y deberá citar la fuente donde la obtuvo mencionando el autor o autores. Cualquier uso distinto como el lucro, reproducción, edición o modificación, será perseguido y sancionado por el respectivo titular de los Derechos de Autor.

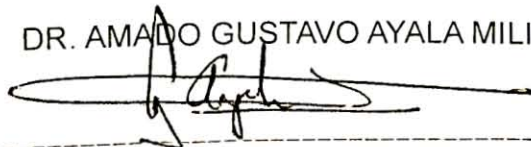
JURADO ASIGNADO:

Presidente: DR. FERNANDO PEÑA MONDRAGÓN
Secretario: DR. JAIME RETAMA VELASCO
Vocal: DR. AMADO GUSTAVO AYALA MILIÁN
1^{er}. Suplente: DR. AGUSTÍN ORDUÑA BUSTAMANTE
2^do. Suplente: DR. GELACIO JUÁREZ LUNA

Lugar o lugares donde se realizó la tesis: INSTITUTO DE INGENIERÍA, UNAM

TUTOR DE TESIS:

DR. AMADO GUSTAVO AYALA MILIÁN

A handwritten signature in black ink, appearing to read 'Amado', is written over a horizontal dashed line. The signature is fluid and cursive.

FIRMA

To Miriam

Acknowledgments

Firstly, I want to express all my gratitude and admiration to Dr. Gustavo Ayala, for sharing his knowledge with me, for his patience, encouragement and availability to guide me. I really appreciate that he trusted in me from the beginning of this work. I am especially grateful with him, for giving me the opportunity to continue working under his supervision.

My sincere thanks to Dr. Jaime Retama, for his advices, valuable ideas and shared knowledge. Also thanks to him for motivating me, for his concern in the progress of this research and his availability for discussing the results of this thesis.

I am totally grateful with Dr. Agustín Orduña, for his guidance and friendly orientation in several aspects of my academic studies and for being a key part of them. I really appreciate all the support given and shared knowledge, essential for the development of this thesis.

I would like to thank the members of my thesis committee: Dr. Gelacio Juárez and Dr. Fernando Peña, for their insightful comments and patience for reviewing this document.

All my gratitude to my family, particularly to my parents and examples of life Ramona Rivera and Armando Amezcua, for supporting me in every decision I made in my life. They trust in me, motivate me and, especially, they instilled in me a value that has brought me here, the work.

My gratitude to Miriam leaves me totally speechless. I am very fortunate for having a person in my life who always supports me in spite of all the sacrifices. A person who always has the exact words of encouragement I need, and gives me the strength to go on. She means everything to me.

Thanks to my colleagues, classmates and friends Isaías Hernández and Gerardo Zamora for both academic and social supports.

This thesis was carried out at the *Instituto de Ingeniería* (IINGEN) of the *Universidad Nacional Autónoma de México* (UNAM) under the supervision of Dr. Gustavo Ayala. This research was possible thanks to the scholarship given by the *Consejo Nacional de Ciencia y Tecnología* (CONACyT).

Abstract

Structural analysis of ancient masonry constructions is a complicated task, generally this is due to the mechanical characteristics of masonry as a structural material and the irregular geometry of these structures. Nowadays, a solution strategy is the use of numerical methods which approximate the solution using computational tools. These methods idealize the irregular geometry of a structure through its discretization as an assemblage of elements of simpler geometry. For masonry structures, its complex mechanical behaviour is implemented by ad hoc constitutive models. Obviously, this strategy involves a high computational cost, which generally leads to the use of simplifying hypothesis upon the behaviour of the problem, which may, nevertheless, drastically impact the accuracy of the results obtained.

In this thesis, two alternatives for the reduction of the computational cost of the structural analysis of historic masonry are investigated: the use of rigid block models and the use of solid finite elements based on a sub-integration scheme with hourglass control. Both investigated approaches reduce the computational cost, nevertheless their foundations and approximation obtained are different. In the former alternative a structure is modeled as a set of rigid blocks interacting through plane interfaces and that, in a two-dimensional case, each has three degrees of freedom, which can be a macro-block composed by a portion of masonry with similar behaviour. Under certain conditions, this modeling process is simpler and the computing time is lower than in finite element method. Nevertheless, this strategy still involves some unsolved issues, discussed in this thesis and for which the formulation is reviewed and applied to one example.

The alternative of using sub-integration in the formulation of solid finite elements is studied, implemented, validated and applied. Considering that the computational cost of forming a stiffness matrix of a solid element is proportional to the number of integration points used, using a low-order integration rule is optimal. However, the use of such a rule may lead to instabilities, known as the hourglass effect. To eliminate this effect and take advantage of the use of sub-integration, a needed stabilization procedure is used. Furthermore, due to the improvements on the characteristics of the stiffness matrix of an element, as the better representation of the strain-energy contributed by the flexural modes, this strategy allows the use of coarser meshes. A full study of this strategy is presented, including a review of the formulation, its numerical implementation in the *Finite Element Analysis Program (FEAP)* and validation examples. The advantages of using this strategy are described and discussed throughout this thesis.

Resumen

El análisis estructural de construcciones antiguas de mampostería es una tarea complicada, generalmente esto se debe a las características mecánicas de la mampostería como material estructural y a la geometría irregular que presentan. En la actualidad, una estrategia de solución es el uso de métodos numéricos que aproximan la solución mediante herramientas computacionales. Estos métodos idealizan la geometría irregular de una estructura mediante su discretización en un ensamble de elementos de geometría más simple. Para estructuras de mampostería, su comportamiento mecánico complejo se implementa mediante modelos constitutivos ad hoc. Obviamente, esta estrategia involucra un costo computacional alto, lo cual generalmente lleva al uso de hipótesis que simplifican el comportamiento del problema, que puede, sin embargo, afectar drásticamente la exactitud de los resultados.

En esta tesis, dos alternativas para la reducción del costo computacional del análisis estructural de mampostería histórica son investigadas: el uso de modelos de bloques rígidos y el uso de elementos finitos sólidos basados en un esquema de subintegración con control del efecto *hourglass*. Ambos enfoques reducen el costo computacional, sin embargo sus fundamentos y aproximaciones obtenidas son diferentes. En la primera alternativa la estructura se modela como un arreglo de bloques rígidos interactuando mediante interfaces planas los cuales, en un caso bidimensional, tienen tres grados de libertad y pueden ser macro bloques compuestos por una porción de mampostería con comportamiento similar. En ciertas condiciones, el proceso de modelado es más simple y el tiempo de cálculo es menor que en el método de elementos finitos. Sin embargo, esta estrategia involucra algunos inconvenientes aún sin resolver, analizados en esta tesis y por los que se revisa la formulación y se aplica a un ejemplo.

La alternativa de usar subintegración en la formulación de elementos finitos sólidos es estudiada, implementada, validada y aplicada. Considerando que el costo computacional de formar una matriz de rigidez de un elemento sólido es proporcional al número de puntos de integración utilizados, el uso de una regla de integración de orden inferior es óptimo. Sin embargo, esto conduce a inestabilidades, conocidas como efecto *hourglass*. Para eliminar este efecto y tomar ventaja del uso de la subintegración, es necesario utilizar un procedimiento de estabilización. Además, debido a mejoras en las características de la matriz de rigidez de un elemento, como la mejor representación de la energía de deformación contribuida por los modos de flexión, esta estrategia permite el uso de mallas más gruesas. Se presenta un estudio completo de esta estrategia, incluyendo una revisión de la formulación, implementación numérica en el programa *FEAP* y ejemplos de validación. Las ventajas de utilizar esta alternativa se describen y discuten a lo largo de la tesis.

Contents

List of Figures	xi
List of Tables	xiii
1 Introduction	1
1.1 Outline of the thesis	2
2 Problem Statement	5
2.1 Introduction	5
2.2 Reduced integration in the finite element method	6
2.3 Objectives	8
2.3.1 Main objective	8
2.3.2 Specific objectives	8
3 Rigid Block Models	9
3.1 Introduction	9
3.2 Formulation	9
3.3 Application example	12
4 Finite Element Method	17
4.1 Introduction	17
4.2 Isoparametric formulation of a quadrilateral element	17
4.2.1 Kinematics	17
4.2.2 Stress-strain relationship	19
4.2.3 Stiffness matrix	20
4.3 Numerical integration	20
4.3.1 Full integration	21
4.3.2 Reduced integration	23
4.4 Hourglass control	24
5 Numerical Implementation	31
5.1 Introduction	31
5.2 Programming	31
5.2.1 One-point stiffness matrix	31
5.2.2 Stabilizer stiffness matrix	33
5.2.3 Stabilized stiffness matrix	33

CONTENTS

5.2.4	Strain matrix	34
5.2.5	Stress matrix	34
5.2.6	Constitutive model	34
5.2.7	Residual	34
6	Validation Examples	37
6.1	Introduction	37
6.2	Cook's membrane (linear case)	38
6.3	Cook's membrane (nonlinear case)	41
7	Application Examples	45
7.1	Introduction	45
7.2	Shear wall with openings	45
7.3	Monastery of São Vicente de Fora	49
7.4	Discussion of results	53
8	Comments and Conclusions	55
8.1	Future works	56
A	The Framework Method	59
A.1	Introduction	59
A.2	Numerical methods	59
A.3	Formulation	60
A.4	Application example	63
	References	67

List of Figures

1.1	Two examples of ancient masonry buildings in Chichén-Itzá, Mexico: (a) the Mayan Observatory and the (b) Pyramid of Kukulkan	1
2.1	Arcade detail of the monastery of São Vicente de Fora: (a) photography, (b) rigid block model and (c) finite element mesh (Orduña et al., 2007)	6
3.1	Interface element and adjacent blocks i and j (Orduña and Ayala, 2016)	11
3.2	Cook’s membrane geometry	12
3.3	Cook’s membrane convergence to analytical solution by rigid block models in (a) strain energy and (b) free-end displacement	13
3.4	Deformation mode 1 of Cook’s membrane analyzed with: (a) finite element method and (b) rigid block model	14
3.5	Deformation mode 2 of Cook’s membrane analyzed with: (a) finite element method and (b) rigid block model	14
3.6	Deformation mode 3 of Cook’s membrane analyzed with: (a) finite element method and (b) rigid block model	15
4.1	4-node quadrilateral element in (a) global coordinates x and y , and (b) natural coordinates ξ and η	18
4.2	4-node quadrilateral element	22
4.3	Deformation modes of the fully-integrated stiffness matrix, $\mathbf{K}_{(4)}$	22
4.4	Deformation modes of the one-point stiffness matrix, $\mathbf{K}_{(1)}$	23
4.5	Deformation modes of the one-point-stabilized stiffness matrix, \mathbf{K}	29
5.1	<i>FEAP</i> (Taylor, 2014) user element routine flowchart	32
5.2	Return mapping algorithm for plane stress elastoplasticity (Simo and Taylor, 1986)	35
6.1	Cook’s membrane geometry	37
6.2	Deformation mode 1 of Cook’s membrane analyzed with: (a) full, (b) reduced and (c) reduced and stabilized numerical integration scheme	38
6.3	Deformation mode 2 of Cook’s membrane analyzed with: (a) full, (b) reduced and (c) reduced and stabilized numerical integration scheme	38
6.4	Deformation mode 3 of Cook’s membrane analyzed with: (a) full, (b) reduced and (c) reduced and stabilized numerical integration scheme	39

LIST OF FIGURES

6.5	Cook's membrane convergence to analytical solution in (a) strain energy and (b) free-end displacement	40
6.6	Cook's membrane (a) A mesh and (b) B mesh	41
6.7	Von Misses stress distribution of Cook's membrane analyzed with A mesh by (a) sub-integration and (b) full-integration; and B mesh by (c) sub-integration and (d) full-integration	42
6.8	Cook's membrane reaction-displacement diagram	43
7.1	Shear wall with openings (a) A mesh and (b) B mesh	46
7.2	Shear wall with openings displacement-reaction diagram	46
7.3	Von Misses stress distribution of shear wall with openings analyzed with A mesh by (a) reduced and (b) full numerical integration	47
7.4	Von Misses stress distribution of shear wall with openings analyzed with B mesh by (a) reduced and (b) full numerical integration	48
7.5	Full-scale model at the ELSA Laboratory (Pegon et al., 2001)	49
7.6	Arcade of monastery of São Vicente de Fora (a) A mesh and (b) B mesh	50
7.7	Arcade of monastery of São Vicente de Fora displacement-reaction diagram	50
7.8	Von Misses stress distribution of the arcade of monastery of São Vicente de Fora analyzed with A mesh by (a) reduced and (b) complete numerical integration	51
7.9	Von Misses stress distribution of the arcade of monastery of São Vicente de Fora analyzed with B mesh by (a) reduced and (b) complete numerical integration	52
A.1	Square pattern of framework for (a) $\nu \neq \frac{1}{3}$ (b) $\nu = \frac{1}{3}$	61
A.2	Timoshenko's column geometry	63
A.3	Timoshenko's column mesh with 4 unit cells at the free end	64
A.4	Deformation modes 1(a,b), 2(c,d), and 3(e,f) of Timoshenko's column solved with: (a,c,e) finite element method and (b,d,f) framework method	64
A.5	Timoshenko's column convergence of the framework method to analytical solution in strain energy	65

List of Tables

- 4.1 Sampling points and weights of the the Gauss-Legendre quadrature (Zienkiewicz and Taylor, 2000) 21
- 4.2 Base vectors of the 4-node quadrilateral element 24
- 4.3 Constants for the stabilization matrix for assumed strain elements (Belytschko and Bindeman, 1991) 28

Introduction

In architectural heritage, are reflected both evolution of construction techniques and knowledge acquisition of structural conception by the human being. The study of structural analysis strategies of historic masonry is justified through the interest of preserving this patrimony, which represents a way to build at a specific time and at certain place. Moreover, many of these buildings are a success, from the architectural and structural point of view, for the time that they were erected (García, 2012).

In Mexico and around the world are scattered pieces of this majestic legacy, which is important to be preserved. For instance, the Mayan Observatory (fig. 1.1a) and the Pyramid of Kukulcan (fig. 1.1a) in Chchén-Itzá, Yucatán, México. This preservation should not only be from an aesthetic viewpoint, actually the essential factor is the structural stability of the building.



(a)



(b)

Figure 1.1: Two examples of ancient masonry buildings in Chichén-Itzá, Mexico: (a) the Mayan Observatory and the (b) Pyramid of Kukulcan

Commonly, several historical constructions are structurally vulnerable, since they have been damaged by strong earthquakes. Therefore, the structural assessment and reinforcement of these buildings have attracted the attention of many researchers and engineers around the world, who are focused in the development and application of new analysis strategies, or the improvement of existing ones.

Regardless the strategy selected, a high computational cost is required for performing a structural analysis of this type of constructions. The study of techniques for reducing this computational cost is justified by the need of having practical tools for the structural diagnosis. Furthermore, the computing-time reduction can lead to the development of more sophisticated constitutive models to obtain better approximations. In this thesis, one of these techniques, based in the use of reduced numerical integration within the finite element method, is studied, validated, implemented and applied to problems which represent ancient buildings. Also, an additional strategy based in rigid block models, is briefly studied and applied to one example.

1.1 Outline of the thesis

In the following paragraphs, a general description of the content of each chapter is presented.

In chapter 2 the problem statement is defined. A general review of some existing strategies for reducing the computational cost of performing a structural analysis is included, remarking the drawbacks and advantages of each one. The main objective and specific objectives of this research, are listed.

The chapter 3 is an overview of the formulation of rigid block models. These models are aimed to the structural assessment of historic masonry. A problem with known solution is analyzed with this strategy. The results of a convergence test and an eigen-analysis are showed and discussed. Finally, interesting remarks are commented.

A study of the selected sub-integration scheme within the finite element method, for the computational cost reduction, is presented in chapter 4. Undesirable effects of using a one-point integration rule, for obtaining the stiffness matrix of a 4-node quadrilateral element, are discussed. A comparison between the eigen-analysis results over the fully-integrated and sub-integrated stiffness matrix is included, focusing in the zero-energy deformation modes. A method to control these effects is studied and validated at level of a single element. The results are widely reviewed.

The numerical implementation of this method is described in chapter 5. An analysis of each step of the algorithm coded in the *FEAP* (Taylor, 2014) program is included. The plasticity constitutive model, employed for the simulation of nonlinear material behaviour, is briefly summarized. In order to validate the reduced integration scheme and the implemented algorithm, for both linear and nonlinear cases, two examples are analyzed in chapter 6. For validation purposes, the results in linear case are compared to the known solution of the problem, and for nonlinear case the comparison is to the ones obtained with full-integration. Highly attractive advantages and interesting remarks are extensively discussed.

Application examples are included in chapter 7. Two buildings, aimed to represent ancient masonry constructions, are analyzed with nonlinear material behaviour. The assay

of these examples is performed by using the sub-integration scheme, studied in this work, and the full-integration scheme conventionally used. A thorough discussion of the results comparison is presented, focusing in the advantages and drawbacks of each scheme.

In chapter 8, final remarks and conclusions derived from this research are discussed. Suggested future works, which can be developed from the results obtained, are included in a final section of this chapter.

Finally, an overview of the framework method is added in the appendix A. Here, the formulation is briefly reviewed and applied to one example with known solution. The results of a convergence test and eigen-analysis are discussed.

Problem Statement

2.1 Introduction

Historically, masonry has been used as the main structural material in diverse buildings or monuments. Along the time, these constructions have deteriorated due to multiple reasons, including the seismic events to which they were subjected. For this reason, it is necessary an assessment of the constructions that are still preserved and determining whether they are stable or no, in structural terms.

Although empirical rules were enough to built these admirable constructions, the application of modern concepts of mechanics and the development of tools for the structural analysis of ancient masonry constructions have been the topic of very active research mainly in the past decades (Orduña, 2003). Generally, this is due to their geometry and the mechanical characteristics of the masonry as a structural element.

Both the properties of the constituent materials and the geometrical arrangement define the masonry overall performance. Masonry is a building material composed of pieces attached by joints with or without mortar. From a geometrical point of view, the historic masonry can be classified into regular and irregular. While the former has a definite-periodic arrangement, the latter does not have any particular geometric pattern (Orduña et al., 2004a).

Generally, the unreinforced masonry presents a very low resistance to tension stresses and a quasi-fragile failure mode, which implies a nonlinear behaviour from small load intensities, not only compared with ultimate loads, but also with the service loads (Orduña et al., 2005). Furthermore, it is a heterogeneous and orthotropic material, due to weakness planes that the joints form (Dhanasekar et al., 1985). These mechanical properties, combined with the size and geometry of the historic buildings, lead to that the analysis of these problems becomes complex and with overly large calculation volumes.

Nowadays, there are many strategies for analyzing this type of problems, for example those which are focused in this research: the *Rigid Block Models* and the *Finite Element Method*. These strategies include the implementation of constitutive models to simulate

2. PROBLEM STATEMENT

the mechanical behaviour of masonry, and also they solve the issue of irregular geometry through the discretization of the structure in an assemble of elements with simpler geometry.

An analysis of an application example and a comparison between the two strategies mentioned above, were performed by Orduña et al. (2004a). In this example, a part of the arcade of the monastery of São Vicente de Fora, located in Lisbon, Portugal (fig. 2.1a), was analyzed. A model of rigid blocks interacting through interfaces is showed in fig. 2.1b, while in fig. 2.1c a finite element mesh is illustrated.

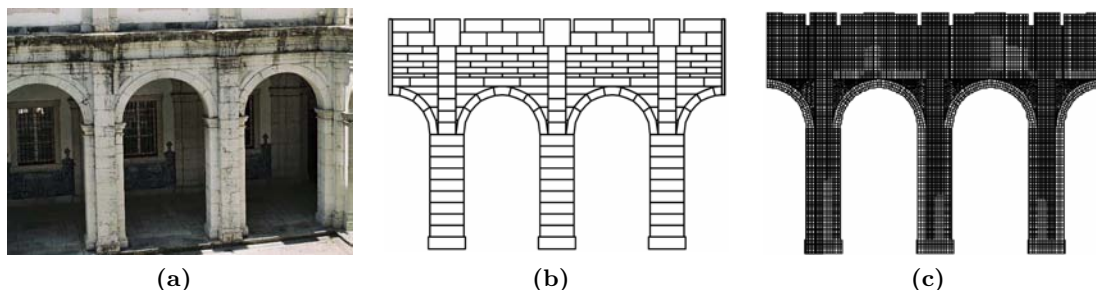


Figure 2.1: Arcade detail of the monastery of São Vicente de Fora: (a) photography, (b) rigid block model and (c) finite element mesh (Orduña et al., 2007)

By comparing figs. 2.1b and 2.1c, it can be noted that the modeling process is easier in the rigid block model. Furthermore, in a rigid block the number of degrees of freedom is smaller than in a finite element. These observations suggest a lower modeling and solving time in rigid block models. Nevertheless, as can be seen in the chapter 3 of this thesis, the convergence of strain energy and displacement is not always to a real solution.

The use of computers, for creating finite element meshes and the numerical analysis, simplifies the development of more sophisticated constitutive models which give results closer to reality. Although the computers are becoming more capable, the computational cost for performing a structural analysis of a complex problem is high, especially in nonlinear cases. Therefore, the development of strategies which reduce the computational cost in the finite element method, is attractive for structural engineers and researchers. For instance, the use of reduced numerical integration to obtain the stiffness matrix.

2.2 Reduced integration in the finite element method

The 4-node quadrilateral isoparametric elements are widely used in computational mechanics. Optimal integration schemes for these elements, however, present a difficult dilemma (Flanagan and Belytschko, 1981). A lower-order quadrature rule, called *reduced integration*, may be desirable for two reasons. First, the reduction of computational cost. This reduction is because the number of evaluations of the compatibility matrix, commonly denoted by a \mathbf{B} , is reduced substantially, especially in non-linear algorithms (Belytschko

et al., 1984). Second, a low-order integration rule tends to soften an element, thus counteracting the excessive stiff behaviour associated with an assumed displacement field. Softening comes about because certain higher-order polynomial terms happen to vanish at Gauss points of a lower-order integration rule, so that these terms make no contribution to strain energy. In other words, with fewer sampling points, some of the more complicated displacement modes offer less resistance to deformation (Cook et al., 1989).

In addition, it was pointed by Wilson et al. (1973) that the isoparametric element, computed by a full-integration rule, does not accurately represent the flexural deformation modes. These fully integrated continuum elements tend to lock if the behavior of the material becomes incompressible (Belytschko et al., 1984).

For these reasons, for large-scale calculations, one-point quadrature elements are attractive because of their speed and accuracy. However, these elements require stabilization. The principal drawback of a reduced integration is the instability that presents in some deformation modes, commonly called *hourglass* effect. The hourglass effect first appears in hydrodynamics applications of the finite difference method (Belytschko et al., 2013).

The hourglass modes are often a nuisance in numerical codes in which the stiffness matrix is calculated by a one-point quadrature integration rule. This is because the stiffness matrix is singular with respect to the hourglass patterns and is non-singular only with respect to the constant strain modes. The obvious way to overcome this problem is to use a full-integration rule. However, a large increase in computational effort is entailed (Kosloff and Frazier, 1978). Numerous techniques have been developed for the control of this effect (Belytschko et al., 1984).

Attempts to deal with this phenomenon appear first in finite difference literature where Maenchen and Sack (1964) added artificial viscosity to inhibit opposing rotations of the sides. Furthermore, the hourglass viscosity were not independent of the uniform strain and rigid body modes of the element, which could degrade the solution (Flanagan and Belytschko, 1981).

Wilkins et al. (1975) developed a triangular hourglass viscosity for the hexahedron element. This technique is quite complex, involves considerable coding and computation, and is not independent of the deformation and rigid body modes (Flanagan and Belytschko, 1981).

Kosloff and Frazier (1978) proposed a simple scheme to control the hourglass instabilities by adding an hourglass response term to a non-point quadrature stiffness matrix. This derivation is for the isotropic linear elastic case and appears to be relatively economical for even in the most severe cases.

Flanagan and Belytschko (1981) developed a technique for precisely isolating the orthogonal hourglass mode shapes for both quadrilateral elements of arbitrary geometry. This technique is studied in this research.

2.3 Objectives

2.3.1 Main objective

The main objective of this thesis is to numerically implement, validate and apply to nonlinear structural analysis problems of ancient masonry constructions, a 4-node quadrilateral finite element formulation, in which a reduced numerical integration scheme with hourglass control is used in order to obtain an improved stiffness matrix.

2.3.2 Specific objectives

- Study and apply a structural analysis strategy of ancient masonry constructions based in rigid block models.
- Study, numerically implement in the *FEAP* (Taylor, 2014) program environment and validate, for linear analysis, a finite element formulation based in the use of reduced numerical integration.
- Formulate, numerically implement in the *FEAP* (Taylor, 2014) program environment and validate, for nonlinear analysis, this scheme of sub-integration with a constitutive model of plasticity with hardening.
- Apply the strategy studied to models which represent ancient masonry constructions, discussing the advantages and drawbacks of its application.

Rigid Block Models

3.1 Introduction

In this chapter, a formulation based in rigid block models is reviewed. All the information summarized in the first section is proposed by Orduña and Ayala (2016). An application example with known solution is analyzed, applying the formulation described, in order to show the advantages and drawbacks of this strategy. The results in energy and displacement convergence to analytical solution are included. Furthermore, an eigen-analysis is carried out over the stiffness matrix, and the resulting deformation modes are compared to the ones obtained with the finite element method. Finally, several remarks are discussed.

3.2 Formulation

This strategy consists on modeling a structure as a set of rigid blocks interacting through plane interfaces. The blocks are perfectly rigid, therefore, they do not contribute to the deformation of the model. The interfaces concentrate all the strains into their relative displacements. From an structural modeling point of view, the blocks are regarded as extended nodes and the interfaces are the structural elements (Orduña and Ayala, 2016).

The virtual work principle is established at eq. 3.1. Here, $\bar{\boldsymbol{\varepsilon}}$ are the virtual strains inside blocks; $\bar{\mathbf{q}}$ are the relative virtual displacements at the interfaces; $\bar{\mathbf{u}}$ are the virtual displacements inside the blocks and $\bar{\mathbf{u}}_{S_f}$ are the virtual displacements at the model surfaces subject to external loads, \mathbf{f}_{S_f} . Also, $\boldsymbol{\sigma}$ are the stresses inside the blocks; \mathbf{Q} are the tractions at interface surfaces, S_I , and \mathbf{f}_B are the body forces acting inside the blocks (Orduña and Ayala, 2016).

$$\int_{V_m} \bar{\boldsymbol{\varepsilon}}^T \boldsymbol{\sigma} dV + \int_{S_I} \bar{\mathbf{q}}^T \mathbf{Q} dS = \int_{V_m} \bar{\mathbf{u}}^T \mathbf{f}_B dV + \int_{S_f} \bar{\mathbf{u}}_{S_f}^T \mathbf{f}_{S_f} dS \quad (3.1)$$

For a two-dimensional case, the kinematics of each block is defined by 3 degrees of freedom of its centre of mass, two of them are translational and the other rotational (Orduña et al., 2007). In a three-dimensional case, per block there are 6 degrees of freedom, 3

3. RIGID BLOCK MODELS

translational and 3 rotational. The relative displacements at any interface point are given by the following expression (Orduña and Ayala, 2016):

$$\mathbf{q}_e = \mathbf{B}_e \mathbf{U}_e \quad (3.2)$$

where \mathbf{B}_e is a compatibility matrix which depends on the geometric characteristics of the involved blocks and interfaces and \mathbf{U}_e are the displacements of the adjacent blocks. Eq. 3.3 expresses the relationship between tractions and relative displacements at a point in the interface, through the constitutive matrix, \mathbf{C}_e (Orduña and Ayala, 2016).

$$\mathbf{Q}_e = \mathbf{C}_e \mathbf{q}_e \quad (3.3)$$

The displacements of an arbitrary point inside a particular block relate to the displacements of the block centre of mass by eq. 3.4. Matrix \mathbf{H}_b depends on the block geometry (Orduña and Ayala, 2016).

$$\mathbf{u}_b = \mathbf{H}_b \mathbf{U}_b \quad (3.4)$$

Using eqs. 3.2, 3.3 and 3.4 in eq. 3.1 and simplifying, eq. 3.5 is obtained. This expression is the characteristic equation of the displacement method (Orduña and Ayala, 2016).

$$\mathbf{K} \mathbf{U} = \mathbf{F}_B + \mathbf{F}_{S_{fb}} = \mathbf{F}_{ext} \quad (3.5)$$

where:

$$\mathbf{K} = \sum_e \int_{S_{Ie}} \mathbf{B}_e^T \mathbf{C}_e \mathbf{B}_e dS \quad (3.6)$$

$$\mathbf{F}_B = \sum_e \sum_b \int_{V_b} \mathbf{H}_b^T \mathbf{f}_B dV \quad (3.7)$$

$$\mathbf{F}_{S_{fb}} = \sum_b \int_{S_{fb}} \mathbf{H}_b^T \mathbf{f}_{S_f} dS \quad (3.8)$$

Thus, the stiffness matrix of an interface element, \mathbf{K} , can be obtained with eq. 3.6. Fig. 3.1 shows a generic interface in the model between two blocks i and j . This figure illustrates the linear degrees of freedom of these two blocks. The rotational degrees of freedom, not shown in the figure, are superposed to the linear ones. The displacement at these degrees of freedom constitute the vector \mathbf{U}_e (eq. 3.9). Variables u , v and w are the displacements of the block centre of mass in the global coordinate directions X , Y and Z respectively. Also, r_x , r_y and r_z are the rotations of the block about the same global coordinate directions. Figure 3.1 also shows the positive directions of the relative displacements of a generic point $p(x, y, z)$ at the interface. Vector \mathbf{q}_e gather these variables (eq. 3.10). Here Δ_{S_1} and Δ_{S_2} are the tangential displacements along the local coordinates x_1 and x_2 , respectively, and Δ_n is the relative normal displacement, positive in tension, when pointing from block i to block j (Orduña and Ayala, 2016).

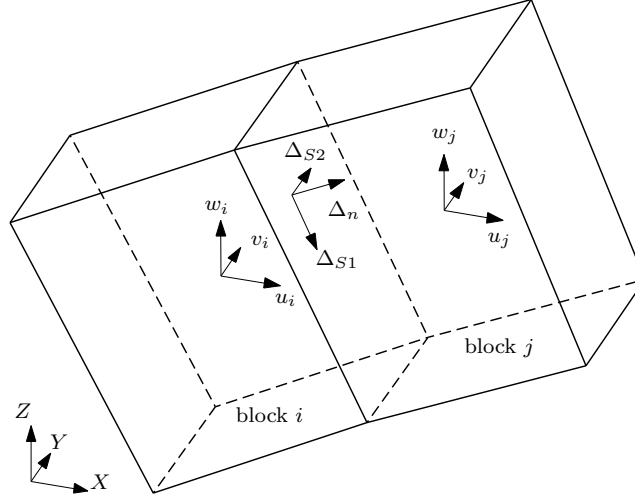


Figure 3.1: Interface element and adjacent blocks i and j (Orduña and Ayala, 2016)

$$\mathbf{U}_e^T = [u_i \quad v_i \quad w_i \quad r_{xi} \quad r_{yi} \quad r_{zi} \mid u_j \quad v_j \quad w_j \quad r_{xj} \quad r_{yj} \quad r_{zj}] \quad (3.9)$$

$$\mathbf{q}_e^T = [\Delta_{S1} \quad \Delta_{S2} \quad \Delta_n] \quad (3.10)$$

In eq. 3.6 appear both, the element compatibility matrix \mathbf{B}_e and the constitutive matrix \mathbf{C}_e . The former, according to eq. 3.2, relates the displacements of the blocks next to the interface, \mathbf{U}_e , to the relative displacements at a point in the interface, \mathbf{q}_e . Equation 3.11 provides the part of this matrix used to obtain the contribution of the block j displacements to the interface relative displacements (eq. 3.11). Here, \mathbf{T}_e^g is the transformation matrix from global to local coordinates; also X_j , Y_j and Z_j are the coordinates of the block j centre of mass. The whole \mathbf{B}_e matrix consists of two sub-matrices like this, one for block i and other for block j , as indicated by eq. 3.12 (Orduña and Ayala, 2016).

$$\mathbf{B}_e^j = \begin{bmatrix} 1 & 0 & 0 & 0 & (z - Z_j) & -(y - Y_j) \\ 0 & 1 & 0 & -(z - Z_j) & 0 & (x - X_j) \\ 0 & 0 & 1 & (y - Y_j) & (x - X_j) & 0 \end{bmatrix} \quad (3.11)$$

$$\mathbf{B}_e = [-\mathbf{B}_e^i \mid \mathbf{B}_e^j] \quad (3.12)$$

Regarding the constitutive matrix, \mathbf{C}_e , which relates the relative displacements at a point on the interface to the corresponding tractions (eq. 3.3), eq. 3.13 is proposed by Orduña and Ayala (2016). Here, E is the Young modulus, while G_1 and G_2 are the shear modulus along the local directions x_1 and x_2 respectively. Also, L_e is a characteristic length, calculated as the normal to interface projection of the distance between the block centres of mass (Orduña and Ayala, 2016).

$$\mathbf{C}_e = \begin{bmatrix} G_1/L_e & 0 & 0 \\ 0 & G_2/L_e & 0 \\ 0 & 0 & E/L_e \end{bmatrix} \quad (3.13)$$

Finally, the integrals indicated in eq. 3.6 are performed by standard numerical integration techniques common in finite element procedures (Orduña and Ayala, 2016).

3.3 Application example

The problem of the Cook's membrane (Cook, 1974) was selected as application example, due to that its analytical solution is known for a linear case. The geometry and restraints are shown in fig. 3.2. For analyzing the membrane, a Young's module $E = 1,000$ MPa, a Poisson's ratio $\nu = 0.33$ and an applied load $P = 1,000$ N in the free end were considered. This load has a parabolic distribution, as shown in fig. 3.2.

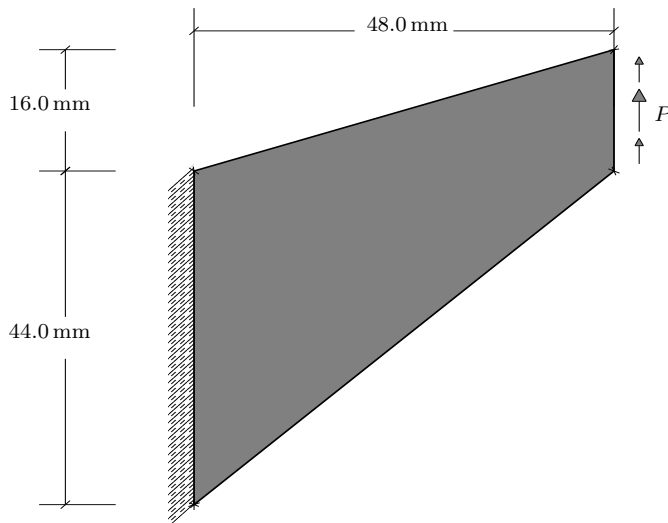
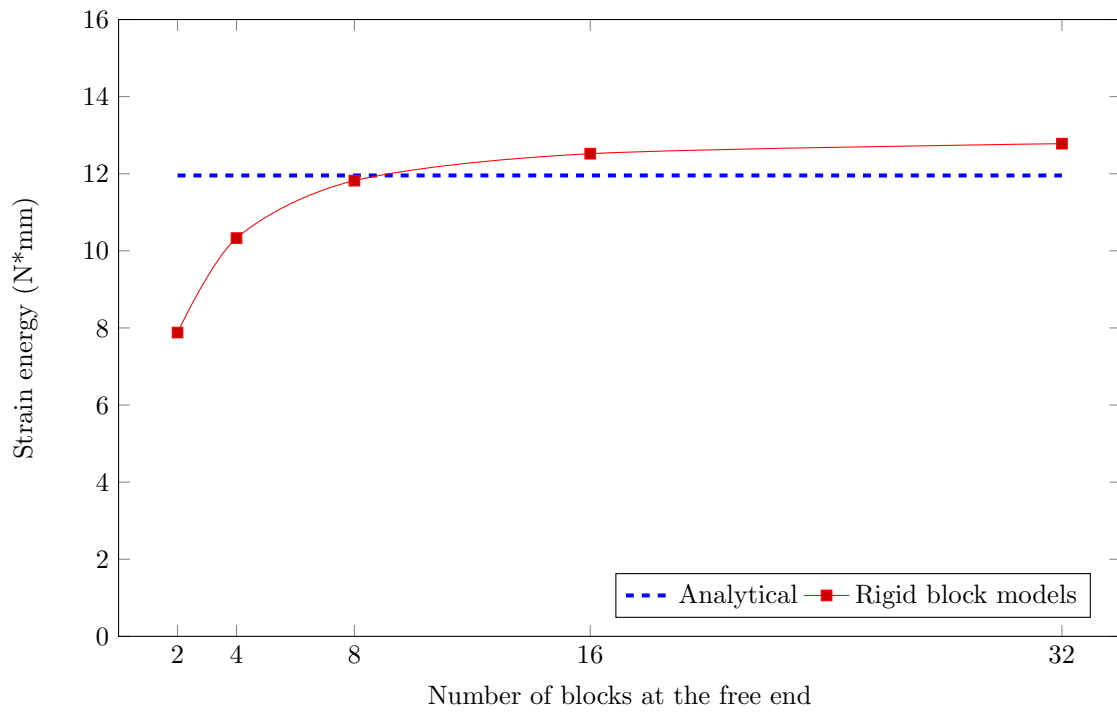


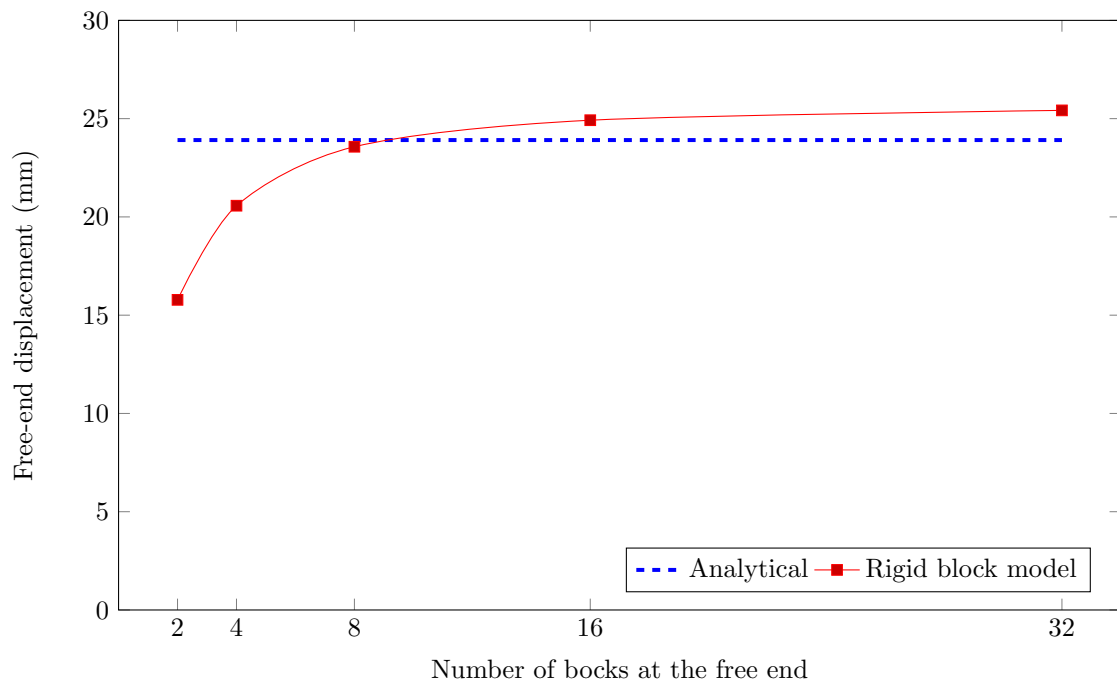
Figure 3.2: Cook's membrane geometry

Five models were built, with 2, 4, 8, 16 and 32 rigid blocks at the end where load is applied. As mentioned above, these blocks interact through plane interfaces. An unitary thickness of the membrane was considered, in order to simulate a two-dimensional problem for comparison purposes, since the analytical solution is given for a plane stress case. The formulation, summarized in the former section, was applied through a software developed by Orduña and Ayala (2016) based on the program *PyFEM* (De Borst et al., 2012).

Figure 3.3a shows the convergence to the analytical solution of strain energy, and in fig. 3.3b to the analytical solution of the free-end displacement. An undesirable behaviour in both figures is observed, since although the solution is converging to a stationary value, this value does not correspond to the analytical solution neither of the strain energy nor the free-end displacement.



(a)



(b)

Figure 3.3: Cook's membrane convergence to analytical solution by rigid block models in (a) strain energy and (b) free-end displacement

3. RIGID BLOCK MODELS

In this example, the difference between the strain energy obtained with the model of 32 rigid blocks at the free end and the analytical solution is 6.90 %. Although this difference does not represent a major problem, the main drawback is that the stationary value of the convergence curve is numerically higher than the analytical solution, which implies that the method is not mathematically optimal for analyzing this type of problems.

The characteristic equation of the global stiffness matrix, $(\mathbf{K} - \lambda\mathbf{I})\Phi = \mathbf{0}$, was also solved. In figs. 3.4 to 3.6, three deformation modes of the model with four rigid blocks in the free end, are compared with the corresponding modes obtained with an analogous mesh of finite elements. Both problems were solved with the same mechanical properties of the material and same boundary conditions. In these graphical representations, same scale factor is used and the out-of-plane modes of the rigid block model are discarded, for comparison purposes.

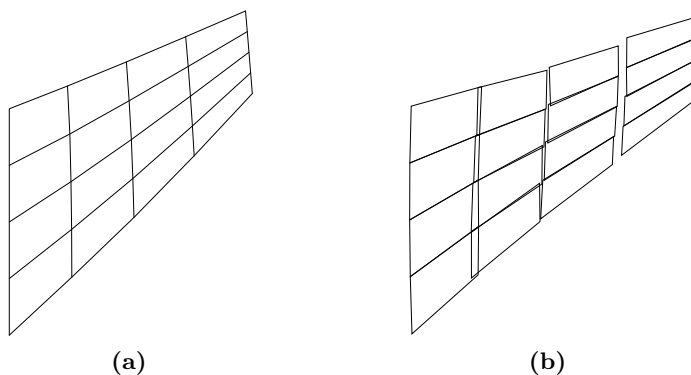


Figure 3.4: Deformation mode 1 of Cook's membrane analyzed with: (a) finite element method and (b) rigid block model

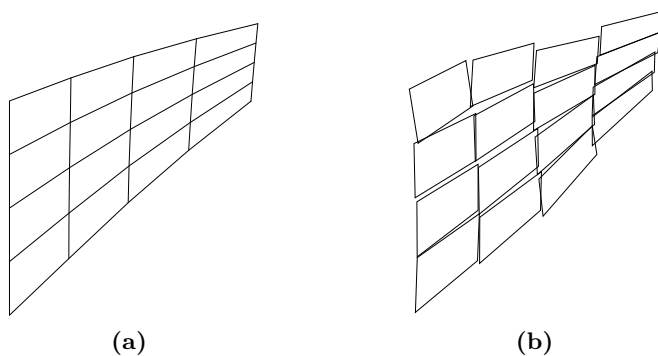


Figure 3.5: Deformation mode 2 of Cook's membrane analyzed with: (a) finite element method and (b) rigid block model

In these figures, a similar mechanism can be seen among all modes. In the modes obtained with the rigid block model, it can be noted that the blocks are detached, something expected since the blocks are rigid, or they are overlapped, which may be difficult to

interpret. However, from a strictly structural viewpoint, this may be interpreted as a compressive strain, since the blocks are regarded as extended nodes and only the interfaces are structural elements, concentrating, as mentioned before, all the strains into their relative displacements.

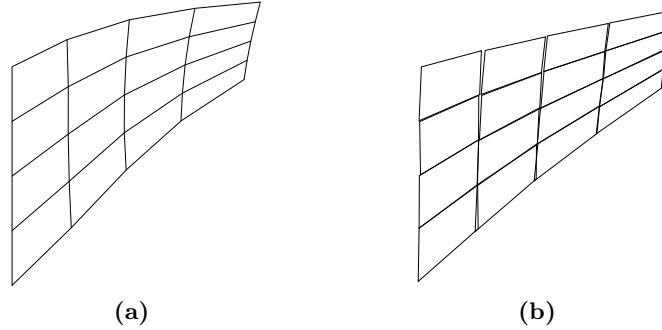


Figure 3.6: Deformation mode 3 of Cook's membrane analyzed with: (a) finite element method and (b) rigid block model

An important fact for explaining the issues presented in this application example is that the Cook's membrane represents a continuum structure, optimal for being solved through the conventional finite element method, that is perfectly aimed to represent this type of structures. Nevertheless, the rigid block models, from their conception, are not focused on continuous structures, since the perfectly rigid blocks are interacting through interfaces, which combined can simulate the structural behaviour of a highly heterogeneous material, as the masonry. Moreover, the fact of considering the masonry as continuum material is under discussion, because in several historical constructions the joining material used to attach the masonry units is strengthless, due to the poor quality materials or the lack of appropriate construction techniques, and in other cases, there is no joining material and the masonry units are attached only by self-weight forces. Orduña and Ayala (2016) validated positively this method through a comparison with experimental results.

In spite of the drawbacks presented at this example, the rigid block models offer a useful result for the structural engineering labor field, especially for the analysis of large structures, in the absence of other computationally economical methods offering an engineering practical application. Even if the results do not represent a real solution, the collapse mechanism approximate in this strategy, can be utilized for detecting where the structure needs to be reinforced.

Several sophisticated models, developed within the finite element method, have demonstrated that they can accurately represent the behaviour of ancient masonry constructions. Nevertheless, the computational cost of carrying out an analysis with these developments is quite high, which makes that their application is only justified in research works and not in the structural engineering labor field. This is one of the reasons for studying a computational cost reduction technique within the finite element method, in order to have an economical and highly-accurate strategy.

Finite Element Method

4.1 Introduction

In this chapter, a one-point integration scheme for the 4-node quadrilateral finite element, is presented as an alternative for reducing the computational cost in structural analysis of ancient masonry constructions. This scheme is based in the control of the hourglass effect by adding a stabilizer matrix to the sub-integrated stiffness matrix.

First, a brief review of the isoparametric formulation for the stiffness matrix obtaining is included. In order to identify the drawbacks of a full or reduced integration rule, an eigen-analysis is performed over the fully-integrated and sub-integrated stiffness matrix of a single element. The effect of the integration rule in the deformation modes is analyzed, and the appearance of hourglass modes discussed.

Finally, a stabilization method for the one-point stiffness matrix is studied and applied to the same element. A discussion of the hourglass modes control is presented.

4.2 Isoparametric formulation of a quadrilateral element

Figure 4.1a shows a 4-node quadrilateral element in global coordinates x and y , and fig.4.1b shows its representation in natural coordinates ξ and η .

4.2.1 Kinematics

As it is an isoparametric formulation, the same shape functions, \mathbf{N} , are used to approximate both the displacement field, \mathbf{u} , and the geometry, \mathbf{X} , of the element. The displacement field and the geometry interpolation approaches to:

$$\mathbf{u} = \begin{bmatrix} u_x \\ u_y \end{bmatrix} = \begin{bmatrix} N_1 & 0 & N_2 & 0 & N_3 & 0 & N_4 & 0 \\ 0 & N_1 & 0 & N_2 & 0 & N_3 & 0 & N_4 \end{bmatrix} \mathbf{d} \quad (4.1)$$

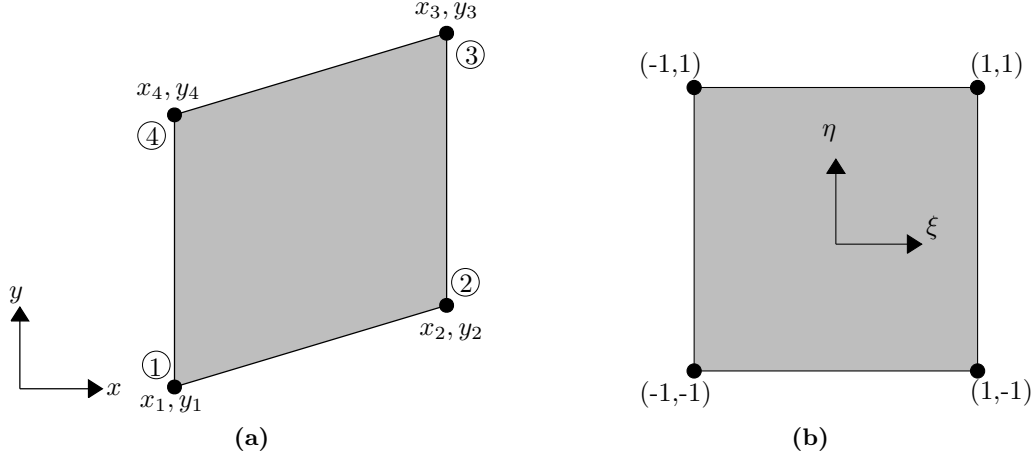


Figure 4.1: 4-node quadrilateral element in (a) global coordinates x and y , and (b) natural coordinates ξ and η

$$\mathbf{X} = \begin{bmatrix} x \\ y \end{bmatrix} = \begin{bmatrix} N_1 & 0 & N_2 & 0 & N_3 & 0 & N_4 & 0 \\ 0 & N_1 & 0 & N_2 & 0 & N_3 & 0 & N_4 \end{bmatrix} \boldsymbol{\chi} \quad (4.2)$$

where \mathbf{d} and $\boldsymbol{\chi}$ are vectors which contain the displacements and the coordinates, in the global system, respectively (eq. 4.3).

$$\mathbf{d}^T = [d_{x1} \ d_{y1} \ d_{x2} \ d_{y2} \ d_{x3} \ d_{y3} \ d_{x4} \ d_{y4}] \quad (4.3a)$$

$$\boldsymbol{\chi}^T = [x_1 \ y_1 \ x_2 \ y_2 \ x_3 \ y_3 \ x_4 \ y_4] \quad (4.3b)$$

The shape functions for the 4-node quadrilateral element (fig. 4.1) are:

$$\mathbf{N} = \begin{bmatrix} N_1 \\ N_2 \\ N_3 \\ N_4 \end{bmatrix} = \frac{1}{4} \begin{bmatrix} (1-\xi)(1-\eta) \\ (\xi+1)(1-\eta) \\ (\xi+1)(\eta+1) \\ (1-\xi)(\eta+1) \end{bmatrix} \quad (4.4)$$

Element kinematics are enforced through strain-deformation equations defined by the symmetric gradient of the displacement field:

$$\boldsymbol{\varepsilon} = \nabla^s \mathbf{u} \quad (4.5)$$

$$\varepsilon_{xx} = \frac{\partial u_x}{\partial x} \quad \varepsilon_{yy} = \frac{\partial u_y}{\partial y} \quad \gamma_{xy} = \frac{\partial u_y}{\partial x} + \frac{\partial u_x}{\partial y} \quad (4.6)$$

Equations 4.6 and 4.1 yield eq. 4.7. By convention, a comma preceding a lowercase subscript denotes differentiation with respect to the global coordinate system x or y .

$$\boldsymbol{\varepsilon} = \begin{bmatrix} \varepsilon_{xx} \\ \varepsilon_{yy} \\ \gamma_{xy} \end{bmatrix} = \underbrace{\begin{bmatrix} \mathbf{N}_{,x} & \mathbf{0} \\ \mathbf{0} & \mathbf{N}_{,y} \\ \mathbf{N}_{,y} & \mathbf{N}_{,x} \end{bmatrix}}_{\mathbf{B}} \mathbf{d} \quad (4.7)$$

For a finite element this means that the strain-displacement relationship is defined as $\boldsymbol{\varepsilon} = \mathbf{B} \mathbf{d}$, where \mathbf{B} is the compatibility matrix that contains the shape functions derivatives with respect to the global coordinate system. Since the shape functions are defined in natural coordinate system, ξ and η , it is necessary to perform a coordinate transformation to obtain the compatibility matrix, \mathbf{B} , with eq. 4.7. The Jacobian matrix, \mathbf{J} , is required (eq. 4.8).

$$\begin{bmatrix} \frac{\partial N_i}{\partial x} \\ \frac{\partial N_i}{\partial y} \end{bmatrix} = \underbrace{\begin{bmatrix} \frac{\partial x}{\partial \xi} & \frac{\partial y}{\partial \xi} \\ \frac{\partial x}{\partial \eta} & \frac{\partial y}{\partial \eta} \end{bmatrix}}_{\mathbf{J}} \begin{bmatrix} \frac{\partial N_i}{\partial \xi} \\ \frac{\partial N_i}{\partial \eta} \end{bmatrix} \quad (4.8)$$

The derivatives of the shape functions with respect to the global coordinate system are calculated as follows:

$$\begin{bmatrix} \frac{\partial N_i}{\partial x} \\ \frac{\partial N_i}{\partial y} \end{bmatrix} = \begin{bmatrix} \frac{\partial x}{\partial \xi} & \frac{\partial y}{\partial \xi} \\ \frac{\partial x}{\partial \eta} & \frac{\partial y}{\partial \eta} \end{bmatrix}^{-1} \begin{bmatrix} \frac{\partial N_i}{\partial \xi} \\ \frac{\partial N_i}{\partial \eta} \end{bmatrix} \quad (4.9)$$

Finally, the compatibility matrix, \mathbf{B} , is obtained by performing a rearrangement of the terms of eq. 4.9.

$$\mathbf{B} = \begin{bmatrix} N_{1,x} & 0 & N_{2,x} & 0 & N_{3,x} & 0 & N_{4,x} & 0 \\ 0 & N_{1,y} & 0 & N_{2,y} & 0 & N_{3,y} & 0 & N_{4,y} \\ N_{1,y} & N_{1,x} & N_{2,y} & N_{2,x} & N_{3,y} & N_{3,x} & N_{4,y} & N_{4,x} \end{bmatrix} \quad (4.10)$$

4.2.2 Stress-strain relationship

The constitutive matrix, \mathbf{C} , relates stresses and strains (eq. 4.11).

$$\boldsymbol{\sigma} = \mathbf{C} \boldsymbol{\varepsilon} \quad (4.11)$$

This matrix depends on the material properties and the type of problem to be analyzed. For a two-dimensional formulation of linearly-elastic solid, the constitutive matrix is:

$$\mathbf{C} = \begin{bmatrix} \bar{\lambda} + 2\mu & \bar{\lambda} & 0 \\ \bar{\lambda} & \bar{\lambda} + 2\mu & 0 \\ 0 & 0 & \mu \end{bmatrix} \quad (4.12)$$

where $\bar{\lambda} = E\nu/(1 - \nu^2)$ for plane stress, and $\bar{\lambda} = \lambda$ for plane strain. The parameters λ

and μ are the Lamé constants, E is the Young's modulus and ν is the Poisson's ratio.

4.2.3 Stiffness matrix

The stiffness matrix, \mathbf{K} , for an element with thickness t and area A , is obtained through eq. 4.13.

$$\mathbf{K} = t \int_A \mathbf{B}^T \mathbf{C} \mathbf{B} dA \quad (4.13)$$

Due to the complexity of solving this expression analytically, numerical integration is used to evaluate it numerically. Since the computational cost of this numerical evaluation is proportional to the number of integration points utilized, the selection of the optimal integration rule is highly important.

4.3 Numerical integration

Quadrature is the name applied to the rule used to evaluate numerically an integral, rather than analytically as is done in tables of integrals. There are many quadrature rules. The Gauss-Legendre rules are most appropriate for 4-node quadrilateral elements. An integral having arbitrary limits can be transformed so that its limits are from -1 to $+1$ (Cook et al., 1989), as follows:

$$I = \int_{x_1}^{x_2} f(x) dx = \int_{-1}^1 \phi(\xi) d\xi \quad (4.14a)$$

$$I = \int_{y_1}^{y_2} \int_{x_1}^{x_2} f(x, y) dx dy = \int_{-1}^1 \int_{-1}^1 \phi(\xi, \eta) d\xi d\eta \quad (4.14b)$$

$$I = \int_{z_1}^{z_2} \int_{y_1}^{y_2} \int_{x_1}^{x_2} f(x, y, z) dx dy dz = \int_{-1}^1 \int_{-1}^1 \int_{-1}^1 \phi(\xi, \eta, \zeta) d\xi d\eta d\zeta \quad (4.14c)$$

where $\phi(\xi)$ incorporates the determinant of the Jacobian matrix of the transformation. To evaluate numerically the integral, the expressions $\phi(\xi_i)$ of eq. 4.14, are evaluated in the sampling points and multiplied by their corresponding weights factors (eq. 4.15).

$$I = \int_{-1}^1 \phi(\xi) d\xi = \sum_{i=1}^n w_i \phi(\xi_i) \quad (4.15a)$$

$$I = \int_{-1}^1 \int_{-1}^1 \phi(\xi, \eta) d\xi d\eta = \sum_{i=1}^n \sum_{j=1}^n w_i w_j \phi(\xi_i, \eta_j) \quad (4.15b)$$

$$I = \int_{-1}^1 \int_{-1}^1 \int_{-1}^1 \phi(\xi, \eta, \zeta) d\xi d\eta d\zeta = \sum_{i=1}^n \sum_{j=1}^n \sum_{k=1}^n w_i w_j w_k \phi(\xi_i, \eta_j, \zeta_k) \quad (4.15c)$$

where w_i , w_j and w_k are the weight factors associated to the n sampling points in the directions of coordinates ξ_i , η_j and ζ_k , respectively. Data of the Gauss-Legendre quadrature appear in table 4.1

Table 4.1: Sampling points and weights of the the Gauss-Legendre quadrature (Zienkiewicz and Taylor, 2000)

n	ξ_i	w_i
1	0	2
2	$\pm 1/\sqrt{3}$	1
3	0.0	8/9
	$\pm\sqrt{1/3}$	5/9
4	± 0.861136311594053	0.347854845147454
	± 0.339981043584856	0.652145154862546
	± 0.906179845938664	0.236926885056189
5	± 0.538469310105683	0.478628670499366
	0.000000000000000	0.586888888888889

When \mathbf{K} is evaluated by means of a numerical integration, it contains only the information that can be sensed at the sampling points of the quadrature rule. If it happens that strains, $\boldsymbol{\varepsilon} = \mathbf{B}\mathbf{d}$, are zero at all sampling points for a certain mode, $\mathbf{d} = \boldsymbol{\phi}$, then the strain energy, U_e , will vanish for that mode, in the sense that $U_e = (1/2)\boldsymbol{\phi}^T \mathbf{K} \boldsymbol{\phi}$ is zero. It is expected that $U_e = 0$ if $\boldsymbol{\phi}$ is a rigid-body motion. If $U_e = 0$ when $\boldsymbol{\phi}$ is not a rigid-body motion, then an instability is present (Cook et al., 1989).

4.3.1 Full integration

For numerically integrated elements, *full integration* is defined as a quadrature rule sufficient to provide the exact value of the integrals for all terms in the element stiffness matrix if the element is not undistorted (Cook et al., 1989). In this case, for a 4-node quadrilateral element, a 2 by 2 quadrature is required for a full integration.

Consider the 4-node quadrilateral element of fig. 4.2 with a Young's module $E = 2,000$ MPa, a Poisson's ratio $\nu = 0.20$ and a global coordinates $\mathbf{x}^T = [0 \ 1 \ 1 \ 0]$ and $\mathbf{y}^T = [0 \ 0 \ 1 \ 1]$. Applying the formulation explained in section 4.2 and evaluating eq. 4.13 with a 2 by 2 quadrature, the fully-integrated stiffness matrix, $\mathbf{K}_{(4)}$, is obtained (eq. 4.16). Hereinafter, the subscript in parentheses indicates the number of integration points used to obtain the matrix concerned.

$$\mathbf{K}_{(4)} = \begin{bmatrix} 972.2 & 312.5 & -555.6 & -104.2 & -486.1 & -312.5 & 69.4 & 104.2 \\ 312.5 & 972.2 & 104.2 & 69.4 & -312.5 & -486.1 & -104.2 & -555.6 \\ -555.6 & 104.2 & 972.2 & -312.5 & 69.4 & -104.2 & -486.1 & 312.5 \\ -104.2 & 69.4 & -312.5 & 972.2 & 104.2 & -555.6 & 312.5 & -486.1 \\ -486.1 & -312.5 & 69.4 & 104.2 & 972.2 & 312.5 & -555.6 & -104.2 \\ -312.5 & -486.1 & -104.2 & -555.6 & 312.5 & 972.2 & 104.2 & 69.4 \\ 69.4 & -104.2 & -486.1 & 312.5 & -555.6 & 104.2 & 972.2 & -312.5 \\ 104.2 & -555.6 & 312.5 & -486.1 & -104.2 & 69.4 & -312.5 & 972.2 \end{bmatrix} \quad (4.16)$$

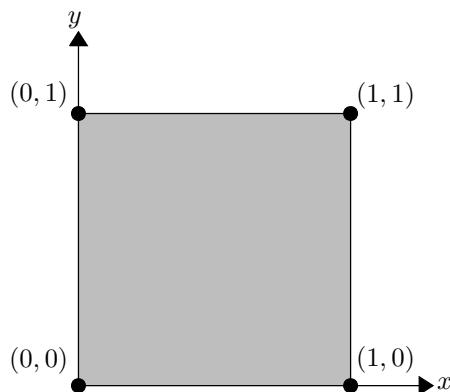


Figure 4.2: 4-node quadrilateral element

The deformation modes of the element can be obtained by solving the characteristic equation of the stiffness matrix, $(\mathbf{K}_{(4)} - \lambda \mathbf{I})\Phi = \mathbf{0}$, where λ is the vector of eigenvalues, \mathbf{I} is the identity matrix and Φ is the matrix of eigenvectors. In fig. 4.3, eight deformation modes for this element can be identified.

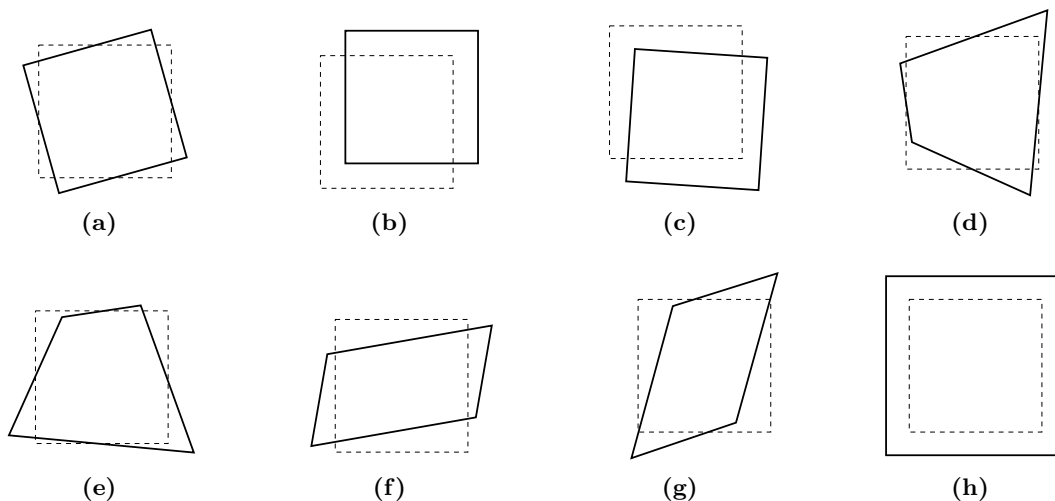


Figure 4.3: Deformation modes of the fully-integrated stiffness matrix, $\mathbf{K}_{(4)}$

The first three are rigid-body modes (figs. 4.3a, 4.3b and 4.3c), i.e., modes for which the strain energy is zero, $U_e = 0$, as it is expected. The next two modes, figs. 4.3d and 4.3e, are bending or linear-strain modes, for which $U_e > 0$. Modes of figs. 4.3f, 4.3g and 4.3h are constant-strain modes, for which $U_e > 0$ (Cook et al., 1989). There are five strain modes (linearly independent) and three rigid-body modes (linearly dependent). By definition, the rank of a matrix is given by the number of columns or rows that are linearly independent. Therefore, the rank of the fully-integrated stiffness matrix is 5.

4.3.2 Reduced integration

A lower-order quadrature rule, called *reduced integration*, may be desirable for two reasons, as described in the chapters 1 and 2. First, since the expense of generating a matrix, \mathbf{K} , by numerical integration is proportional to the number of sampling points, using fewer sampling points means lower cost. Second, a low-order rule tends to soften an element, thus countering the overly stiff behaviour associated with an assumed displacement field. Softening comes about because certain higher-order polynomial terms happen to vanish at Gauss points of a lower-order rule, so that these terms make no contribution to strain energy. In other words, with fewer sampling points, some of the more complicated displacement modes offer less resistance to deformation (Cook et al., 1989).

Consider the same 4-node quadrilateral element that was analyzed with full integration in the preceding section (fig. 4.2). Applying the same formulation, but evaluating eq. 4.13 with a 1 by 1 quadrature, the sub-integrated stiffness matrix, $\mathbf{K}_{(1)}$, is obtained (eq. 4.17).

$$\mathbf{K}_{(1)} = \begin{bmatrix} 729.2 & 312.5 & -312.5 & -104.2 & -729.2 & -312.5 & 312.5 & 104.2 \\ 312.5 & 729.2 & 104.2 & 312.5 & -312.5 & -729.2 & -104.2 & -312.5 \\ -312.5 & 104.2 & 729.2 & -312.5 & 312.5 & -104.2 & -729.2 & 312.5 \\ -104.2 & 312.5 & -312.5 & 729.2 & 104.2 & -312.5 & 312.5 & -729.2 \\ -729.2 & -312.5 & 312.5 & 104.2 & 729.2 & 312.5 & -312.5 & -104.2 \\ -312.5 & -729.2 & -104.2 & -312.5 & 312.5 & 729.2 & 104.2 & 312.5 \\ 312.5 & -104.2 & -729.2 & 312.5 & -312.5 & 104.2 & 729.2 & -312.5 \\ 104.2 & -312.5 & 312.5 & -729.2 & -104.2 & 312.5 & -312.5 & 729.2 \end{bmatrix} \quad (4.17)$$

In fig. 4.4, the eight deformation modes of the one-point stiffness matrix, $\mathbf{K}_{(1)}$, are presented.

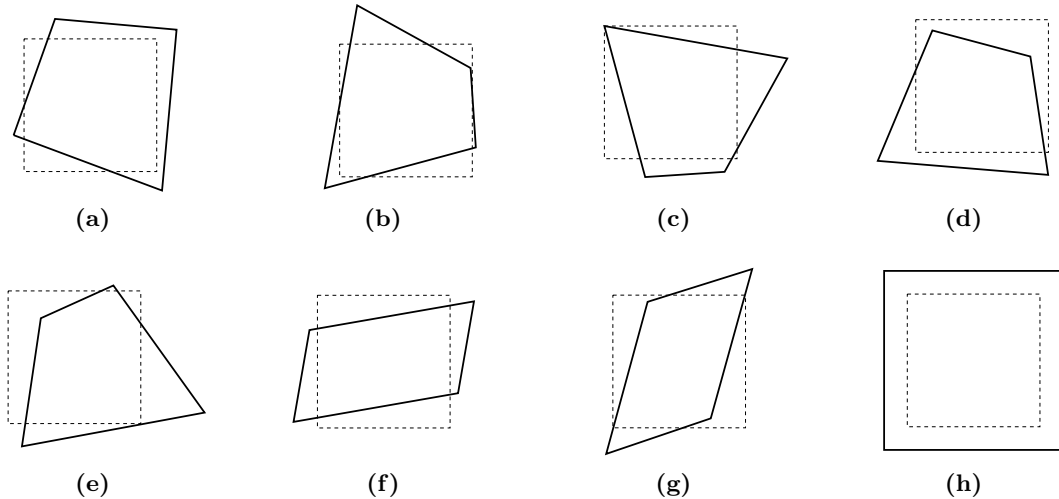


Figure 4.4: Deformation modes of the one-point stiffness matrix, $\mathbf{K}_{(1)}$

The last three are constant-strain modes (figs. 4.4f, 4.4g and 4.4h), for which $U_e > 0$, as it is expected, regardless of the quadrature rule used. For the first five modes, figs.

4.4a to 4.4e, $U_e = 0$, but they are not rigid-body modes. So, an instability is present and these modes are called *spurious* or *hourglass* modes, because of their physical shape when an assembly of elements is performed. Therefore, the rank of the sub-integrated stiffness matrix is 3.

To take advantage of reduced numerical integration, this instability must be eliminated. Through a comparison between fig. 4.4 and fig. 4.3, it may be seen that the modes affected by the hourglass effect are the rigid-body and linear-strain ones, while constant-strain modes are not affected. This is an important fact that is used in the stabilization procedure.

4.4 Hourglass control

An hourglass-control method developed by Belytschko *et al.* (1986; 1991; 2013; 1984; 1981) is studied and implemented in the *FEAP* (Taylor, 2014) program, for the 4-node quadrilateral element analyzed in the preceding sections. This method consists in the addition to the sub-integrated stiffness matrix a stabilizer matrix. This matrix contains the effect of two generalized strains added to control the hourglass modes. Mathematically, the objective is to augment the stiffness-matrix rank from 3 to 5 without affecting the linear fields.

For simplifying the formulation and the expressions utilized, a unique expression that degenerates in the shape functions for each element node can be built using an orthogonal set of base vectors (eq. 4.18 and table 4.2).

$$\mathbf{N} = \frac{1}{4}(1 + \boldsymbol{\xi}\boldsymbol{\xi})(1 + \boldsymbol{\eta}\boldsymbol{\eta}) = \frac{1}{4}(\boldsymbol{\Sigma} + \boldsymbol{\xi}\boldsymbol{\Lambda}_1 + \boldsymbol{\eta}\boldsymbol{\Lambda}_2 + \boldsymbol{\xi}\boldsymbol{\eta}\boldsymbol{\Gamma}) \quad (4.18)$$

Table 4.2: Base vectors of the 4-node quadrilateral element

Node	ξ	η	$\boldsymbol{\Sigma}$	$\boldsymbol{\Lambda}_1$	$\boldsymbol{\Lambda}_2$	$\boldsymbol{\Gamma}$
1	-1	-1	1	-1	-1	1
2	1	-1	1	1	-1	-1
3	1	1	1	1	1	1
4	-1	1	1	-1	1	-1

The above vectors represent the displacement modes of a 4-node quadrilateral element. The first vector, $\boldsymbol{\Sigma}$, accounts for rigid-body translation (fig. 4.3a to 4.3c). The linear base vectors, $\boldsymbol{\Lambda}_1$ y $\boldsymbol{\Lambda}_2$, may be readily combined to define three uniform normal strain modes (fig. 4.3f to 4.3h). The vector $\boldsymbol{\Gamma}$ gives rise to linear strain modes which are neglected when using one-point integration (fig. 4.3d to 4.3e). This vector define the hourglass patterns for the element. Hence, $\boldsymbol{\Gamma}^T = [1 \quad -1 \quad 1 \quad -1]$ is the hourglass base vector (Flanagan and Belytschko, 1981).

Evaluating eq. 4.10 in the sampling point of the one-point quadrature (see table 4.1), the compatibility matrix, $\mathbf{B}_{(1)}$, results:

$$\mathbf{B}(0,0) = \mathbf{B}_{(1)} = \frac{1}{2A} \begin{bmatrix} y_{24} & 0 & y_{31} & 0 & y_{42} & 0 & y_{13} & 0 \\ 0 & x_{42} & 0 & x_{13} & 0 & x_{24} & 0 & x_{31} \\ x_{42} & y_{24} & x_{13} & y_{31} & x_{24} & y_{42} & x_{31} & y_{13} \end{bmatrix} \quad (4.19)$$

where:

$$x_{ij} = x_i - x_j \quad y_{ij} = y_i - y_j \quad (4.20)$$

This matrix can be expressed in terms of two vectors, \mathbf{b}_x and \mathbf{b}_y :

$$\mathbf{B}_{(1)} = \begin{bmatrix} b_{x1} & 0 & b_{x2} & 0 & b_{x3} & 0 & b_{x4} & 0 \\ 0 & b_{y1} & 0 & b_{y2} & 0 & b_{y3} & 0 & b_{y4} \\ b_{y1} & b_{x1} & b_{y2} & b_{x2} & b_{y3} & b_{x3} & b_{y4} & b_{x4} \end{bmatrix} \quad (4.21)$$

where:

$$\mathbf{b}_x^T = \frac{1}{2A} [y_{24} \quad y_{31} \quad y_{42} \quad y_{13}] \quad \mathbf{b}_y^T = \frac{1}{2A} [x_{42} \quad x_{13} \quad x_{24} \quad x_{31}] \quad (4.22)$$

Since $\mathbf{x}^T = [x_1 \quad x_2 \quad x_3 \quad x_4]$ and $\mathbf{y}^T = [y_1 \quad y_2 \quad y_3 \quad y_4]$, it can be easily verified that:

$$\begin{bmatrix} \mathbf{b}_x^T \\ \mathbf{b}_y^T \end{bmatrix} [\mathbf{x} \quad \mathbf{y}] = \begin{bmatrix} 1 & 0 \\ 0 & 1 \end{bmatrix} \quad (4.23)$$

Equation 4.23 is an important requirement for the rows of the matrix $\mathbf{B}_{(1)}$. It is the counterpart of the consistency conditions in finite difference equations; the gradient of a linear field is evaluated properly only if it is satisfied. Additional conditions which can be easily verified are in eq. 4.24. For any undistorted quadrilateral, \mathbf{b}_x , \mathbf{b}_y , $\mathbf{\Sigma}$ and $\mathbf{\Gamma}$ are orthogonal and linearly independent (Belytschko et al., 1984). Eq. 4.24 implies that the matrix $\mathbf{B}_{(1)}$ contains only components of the constant-strain base vectors $\mathbf{\Lambda}_1$ and $\mathbf{\Lambda}_2$ (see fig. 4.4).

$$\begin{aligned} \mathbf{b}_x^T \mathbf{\Sigma} &= 0 & \mathbf{b}_y^T \mathbf{\Sigma} &= 0 \\ \mathbf{b}_x^T \mathbf{\Gamma} &= 0 & \mathbf{b}_y^T \mathbf{\Gamma} &= 0 \\ \mathbf{\Sigma}^T \mathbf{\Gamma} &= 0 \end{aligned} \quad (4.24)$$

The deformation of the element is characterized by velocity strains $\dot{\boldsymbol{\epsilon}} = \mathbf{B}_{(1)} \dot{\mathbf{d}}$. Here, the superposed dots designate time derivatives, and the one-point compatibility matrix, $\mathbf{B}_{(1)}$, for a 4-node quadrilateral is given by eq. 4.21. Using the orthogonality properties of eq. 4.24, it follows immediately that the null space of $\mathbf{B}_{(1)}$ consists of the vectors of eq. 4.25 (Belytschko et al., 1984).

Each column of eq. 4.25 constitutes a separate vector, $\dot{\mathbf{d}}^{<i>}$, so that $\dot{\boldsymbol{\epsilon}} = \mathbf{B}_{(1)} \dot{\mathbf{d}}^{<i>}$ vanishes. The first two vectors are obviously rigid-body (translation) modes (figs. 4.4a and 4.4b) and the third is a rigid-body rotation (fig. 4.4c). The fourth and fifth are spurious singular modes associated with displacement fields for which the strains should

not vanish (figs. 4.4d and 4.4e). Hence the space spanned by the first three vectors of eq. 4.25 is the proper null-space of $\mathbf{B}_{(1)}$; and the remaining two columns constitute the improper null-space, which is of dimension two (Belytschko et al., 1984).

$$\mathbf{d} = \begin{bmatrix} \Sigma_1 & 0 & y_1 & \Gamma_1 & 0 \\ 0 & \Sigma_1 & -x_1 & 0 & \Gamma_1 \\ \Sigma_2 & 0 & y_2 & \Gamma_2 & 0 \\ 0 & \Sigma_2 & -x_2 & 0 & \Gamma_2 \\ \Sigma_3 & 0 & y_3 & \Gamma_3 & 0 \\ 0 & \Sigma_3 & -x_3 & 0 & \Gamma_3 \\ \Sigma_4 & 0 & y_4 & \Gamma_4 & 0 \\ 0 & \Sigma_4 & -x_4 & 0 & \Gamma_4 \end{bmatrix} = \begin{bmatrix} 1 & 0 & y_1 & 1 & 0 \\ 0 & 1 & -x_1 & 0 & 1 \\ 1 & 0 & y_2 & -1 & 0 \\ 0 & 1 & -x_2 & 0 & -1 \\ 1 & 0 & y_3 & 1 & 0 \\ 0 & 1 & -x_3 & 0 & 1 \\ 1 & 0 & y_4 & -1 & 0 \\ 0 & 1 & -x_4 & 0 & -1 \end{bmatrix} \quad (4.25)$$

Therefore, to control the hourglass modes, two additional generalized strains, q , are introduced to the constitutive matrix, \mathbf{C} , which combined with $\mathbf{B}_{(1)}$, span the complement of the proper null-space. The resulting matrix and formula for generalized strains is given by (Belytschko et al., 1984):

$$\mathbf{B}^* = \begin{bmatrix} b_{x1} & 0 & b_{x2} & 0 & b_{x3} & 0 & b_{x4} & 0 \\ 0 & b_{y1} & 0 & b_{y2} & 0 & b_{y3} & 0 & b_{y4} \\ b_{y1} & b_{x1} & b_{y2} & b_{x2} & b_{y3} & b_{x3} & b_{y4} & b_{x4} \\ \gamma_1 & 0 & \gamma_2 & 0 & \gamma_3 & 0 & \gamma_4 & 0 \\ 0 & \gamma_1 & 0 & \gamma_2 & 0 & \gamma_3 & 0 & \gamma_4 \end{bmatrix} \quad (4.26)$$

$$q = \boldsymbol{\gamma}^T \mathbf{d} \quad (4.27)$$

As mentioned before, it is required that the additional strains do not affect linear fields. This requirement automatically leads to a form in which rigid-body rotations are included in the null space. It can be shown that the rows of \mathbf{B}^* are linearly independent for a non-degenerate geometry, so \mathbf{B}^* is of rank 5 and spans the complement of the proper null-space (Belytschko et al., 1984). So, the hourglass shape vector, $\boldsymbol{\gamma}$, is required. The method for controlling the hourglass effect, that is described below, is computationally optimized, i.e., it considers the effect of the hourglass shape vector inside the normally dimensioned compatibility matrix.

One way to obtain the hourglass shape vector, $\boldsymbol{\gamma}$, is to expand the nodal displacement in terms of the translation, constant-gradient and hourglass modes. Since the vectors $\boldsymbol{\Sigma}$, \mathbf{x} , \mathbf{y} and $\boldsymbol{\Gamma}$ are linearly independent (except for distorted elements as shown in eq. 4.24), they span \mathbb{R}^4 (Belytschko and Bindeman, 1991). First, the displacement field can be expressed as:

$$\mathbf{u} = \begin{bmatrix} u_x \\ u_y \end{bmatrix} = \begin{bmatrix} a_{0x} + a_{1x} x + a_{2x} y + a_{3x} h \\ a_{0y} + a_{1y} x + a_{2y} y + a_{3y} h \end{bmatrix} \quad (4.28)$$

where:

$$h = \xi \eta \quad (4.29)$$

This form is complete and satisfies the continuity requirements. The nodal values of \mathbf{d} are those given by Belytschko et al. (1984):

$$\begin{bmatrix} \mathbf{d}_x \\ \mathbf{d}_y \end{bmatrix} = \begin{bmatrix} a_{0x} \boldsymbol{\Sigma} + a_{1x} \mathbf{x} + a_{2x} \mathbf{y} + a_{3x} \boldsymbol{\Gamma} \\ a_{0y} \boldsymbol{\Sigma} + a_{1y} \mathbf{x} + a_{2y} \mathbf{y} + a_{3y} \boldsymbol{\Gamma} \end{bmatrix} \quad (4.30)$$

Multiplying the \mathbf{d}_x expression of 4.30 by \mathbf{b}_x^T and \mathbf{b}_y^T :

$$\begin{bmatrix} \mathbf{b}_x^T \\ \mathbf{b}_y^T \end{bmatrix} \mathbf{d}_x = \begin{bmatrix} \mathbf{b}_x^T \\ \mathbf{b}_y^T \end{bmatrix} (a_{0x} \boldsymbol{\Sigma} + a_{1x} \mathbf{x} + a_{2x} \mathbf{y} + a_{3x} \boldsymbol{\Gamma}) \quad (4.31)$$

Using the orthogonality conditions of eqs. 4.23 and 4.24, eq. 4.31 results:

$$a_{1x} = \mathbf{b}_x^T \mathbf{d}_x \quad a_{2x} = \mathbf{b}_y^T \mathbf{d}_x \quad (4.32)$$

Multiplying the \mathbf{d}_x expression of 4.30 by $\boldsymbol{\Gamma}^T$ and $\boldsymbol{\Sigma}^T$:

$$\boldsymbol{\Gamma}^T \mathbf{d}_x = \boldsymbol{\Gamma}^T (a_{0x} \boldsymbol{\Sigma} + a_{1x} \mathbf{x} + a_{2x} \mathbf{y} + a_{3x} \boldsymbol{\Gamma}) \quad (4.33a)$$

$$\boldsymbol{\Sigma}^T \mathbf{d}_x = \boldsymbol{\Sigma}^T (a_{0x} \boldsymbol{\Sigma} + a_{1x} \mathbf{x} + a_{2x} \mathbf{y} + a_{3x} \boldsymbol{\Gamma}) \quad (4.33b)$$

Using the orthogonality conditions of eqs. 4.23 and 4.24 and substituting the a_{1x} and a_{2x} values in eq. 4.33, the constants a_{0x} and a_{4x} are obtained:

$$a_{3x} = \boldsymbol{\gamma}^T \mathbf{d}_x \quad a_{0x} = \boldsymbol{\Delta}^T \mathbf{d}_x \quad (4.34)$$

where:

$$\boldsymbol{\gamma}^T = \frac{1}{4} \left[\boldsymbol{\Gamma}^T - (\boldsymbol{\Gamma}^T \mathbf{x}) \mathbf{b}_x^T - (\boldsymbol{\Gamma}^T \mathbf{y}) \mathbf{b}_y^T \right] \quad (4.35a)$$

$$\boldsymbol{\Delta}^T = \frac{1}{4} \left[\boldsymbol{\Sigma}^T - (\boldsymbol{\Sigma}^T \mathbf{x}) \mathbf{b}_x^T - (\boldsymbol{\Sigma}^T \mathbf{y}) \mathbf{b}_y^T \right] \quad (4.35b)$$

Equation 4.35a is the $\boldsymbol{\gamma}$ -projection operator of Flanagan and Belytschko (1981). Repeating the same procedure for the y -component, the displacement field of eq. 4.28 becomes eq. 4.36 (Belytschko and Bachrach, 1986).

$$u_x = \mathbf{N} \mathbf{d}_x \quad u_y = \mathbf{N} \mathbf{d}_y \quad (4.36)$$

where:

$$\mathbf{N} = (\boldsymbol{\Delta}^T + x \mathbf{b}_x^T + y \mathbf{b}_y^T + h \boldsymbol{\gamma}^T) \quad (4.37)$$

The symmetric gradient of the displacement field is obtained by taking derivatives of eq. 4.36, which gives (Belytschko and Bindeman, 1991):

$$\nabla^s \mathbf{u} = \begin{bmatrix} u_{x,x} \\ u_{y,y} \\ u_{x,y} + u_{y,x} \end{bmatrix} = \underbrace{\begin{bmatrix} \mathbf{b}_x^T + h_{,x} \gamma^T & \mathbf{0} \\ \mathbf{0} & \mathbf{b}_y^T + h_{,y} \gamma^T \\ \mathbf{b}_y^T + h_{,y} \gamma^T & \mathbf{b}_x^T + h_{,x} \gamma^T \end{bmatrix}}_{\mathbf{B}=\mathbf{B}_{(1)}+\mathbf{B}_{stab}} \begin{bmatrix} \mathbf{d}_x \\ \mathbf{d}_y \end{bmatrix} \quad (4.38)$$

The compatibility matrix in eq. 4.38 is stabilized by the additional terms. The stabilized stiffness matrix, \mathbf{K} , can be obtained through the following expression:

$$\mathbf{K} = \mathbf{K}_{(1)} + \mathbf{K}_{stab} \quad (4.39)$$

where $\mathbf{K}_{(1)}$ is the one-point stiffness matrix, obtained in section 4.3.2, and \mathbf{K}_{stab} is the rank 2 stabilizer stiffness matrix, obtained by solving eq. 4.13 and considering only the additional terms of the compatibility matrix \mathbf{B} (\mathbf{B}_{stab}) in eq. 4.38. The resulting stabilizer matrix is showed in eq. 4.40. It can be noted that each term in this matrix represents a 4-order sub-matrix.

$$\mathbf{K}_{stab} = \begin{bmatrix} -(c_1 H_{xx} + c_2 H_{yy}) \gamma \gamma^T & c_3 H_{xy} \gamma \gamma^T \\ c_3 H_{xy} \gamma \gamma^T & (c_1 H_{yy} + c_2 H_{xx}) \gamma \gamma^T \end{bmatrix} \quad (4.40)$$

where:

$$H_{xx} = \int_A h_{,x}^2 dA \quad H_{yy} = \int_A h_{,y}^2 dA \quad H_{xy} = \int_A h_{,x} h_{,y} dA \quad (4.41)$$

The integrals H_{xx} , H_{yy} and H_{xy} must be calculated with a 2 by 2 quadrature, otherwise they vanish. In eq. 4.40 the terms c_1 , c_2 and c_3 are the constants for the assumed strain elements (Belytschko and Bindeman, 1991). These constants are listed in table 4.3.

Table 4.3: Constants for the stabilization matrix for assumed strain elements (Belytschko and Bindeman, 1991)

Element	c_1	c_2	c_3
Quad4	$\bar{\lambda} + 2\mu$	μ	$\bar{\lambda} + \mu$
SRI	2μ	μ	μ
ASMD	μ	μ	0
ASQBI	$\bar{\lambda}(1 - \bar{\nu})^2 + 2\mu(1 + \bar{\nu}^2)$	0	$\bar{\lambda}(1 - \bar{\nu})^2 - 4\bar{\nu}\mu$
ASOI	4μ	0	-4μ
ASOI(1/2)	μ	0	$-\mu$

In this table $\bar{\nu} = \nu$ for plane stress and $\bar{\nu} = \nu/(1 - \nu)$ for plane strain. Also, Quad4 represents a quadrilateral element without any assumed strain, ASMD is identical to the mean dilatation approach of Nagtegaal et al. (1974), and ASQBI and ASOI are the optimal bending or incompressible elements of Belytschko and Bachrach (1986).

Consider the same 4-node quadrilateral element that was analyzed with full and reduced numerical integration in the preceding sections (fig. 4.2). Applying the stabilization

procedure described in this section, the stabilized stiffness matrix obtained, \mathbf{K} , is:

$$\mathbf{K} = \begin{bmatrix} 983.8 & 312.5 & -567.1 & -104.2 & -474.5 & -312.5 & 57.9 & 104.2 \\ 312.5 & 983.8 & 104.2 & 57.9 & -312.5 & -474.5 & -104.2 & -567.1 \\ -567.1 & 104.2 & 983.8 & -312.5 & 57.9 & -104.2 & -474.5 & 312.5 \\ -104.2 & 57.9 & -312.5 & 983.8 & 104.2 & -567.1 & 312.5 & -474.5 \\ -474.5 & -312.5 & 57.9 & 104.2 & 983.8 & 312.5 & -567.1 & -104.2 \\ -312.5 & -474.5 & -104.2 & -567.1 & 312.5 & 983.8 & 104.2 & 57.9 \\ 57.9 & -104.2 & -474.5 & 312.5 & -567.1 & 104.2 & 983.8 & -312.5 \\ 104.2 & -567.1 & 312.5 & -474.5 & -104.2 & 57.9 & -312.5 & 983.8 \end{bmatrix} \quad (4.42)$$

In fig. 4.5 the eight deformation modes of the one-point-stabilized stiffness matrix, \mathbf{K} , are presented.

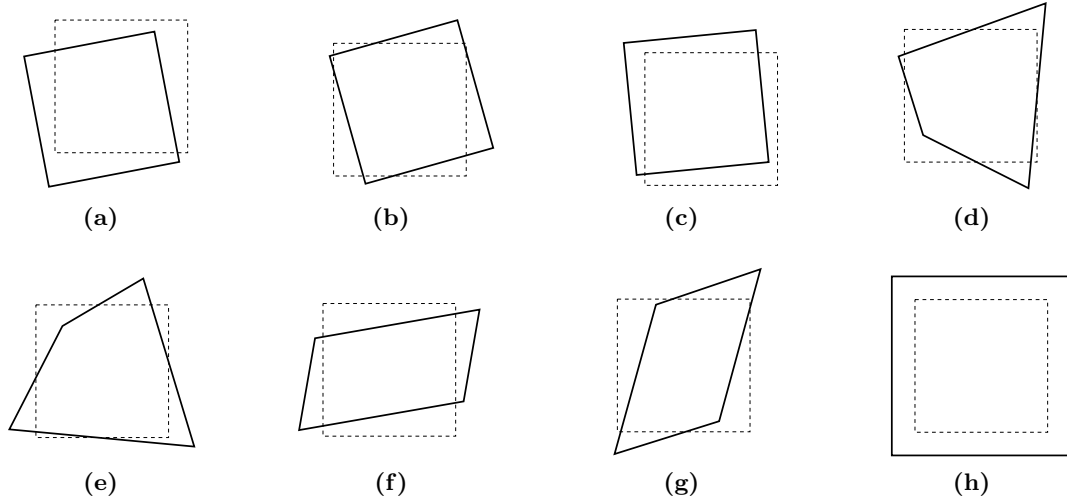


Figure 4.5: Deformation modes of the one-point-stabilized stiffness matrix, \mathbf{K}

As in the fully-integrated stiffness matrix, the first three are rigid-body modes (figs. 4.5a, 4.5b and 4.5c), for which strain energy is zero, $U_e = 0$, the next two modes, figs. 4.5d and 4.5e, are linear-strain modes, for which $U_e > 0$, and modes of figs. 4.5f, 4.5g and 4.5h are constant-strain modes, for which $U_e > 0$. There are five strain modes and three rigid-body modes, therefore the stabilized stiffness matrix rank is 5.

It is proved that the reduced integration scheme, described in this section, correctly augments the rank of the one-point stiffness matrix from 3 to 5. It also controls the hourglass modes, so the instability is no longer present.

Numerical Implementation

5.1 Introduction

In this chapter, a review of the algorithm implemented in the *FEAP* (Taylor, 2014) program is included. To establish all the actions that the routine must perform, for applying the formulation described in the former chapter, a flowchart of the implementation is presented. Each step of the flowchart is explained. Finally, the algorithm of the constitutive model employed is summarized and briefly described.

5.2 Programming

For analyzing models, which represent real structural engineering problem, using the sub-integration scheme described in the past chapter, a numerical implementation in a computational environment is required. For doing this, the open source software *FEAP* (Taylor, 2014) is selected. This program has the advantage of allowing the addition of user element routines.

The implemented element user routine follows the algorithm from the flowchart in fig. 5.1. All the actions performed in each step are described below.

5.2.1 One-point stiffness matrix

The one-point stiffness matrix, $\mathbf{K}_{(1)}$, for each element is computed with eq. 5.1. As in the former chapter, a subscript in brackets indicates the number of integration points utilized in the matrix obtainment.

$$\mathbf{K}_{(1)} = A \mathbf{B}_{(1)}^T \mathbf{C} \mathbf{B}_{(1)} \quad (5.1)$$

Here, A is the element area computed with eq. 5.2, and $\mathbf{B}_{(1)}$ is the compatibility matrix evaluated in the sampling point of a 1 by 1 quadrature ($\xi = 0, \eta = 0$). This matrix is calculated with eq. 5.3 (see eq. 4.19). Also, \mathbf{C} is the plane-stress constitutive matrix (see eq. 4.12).

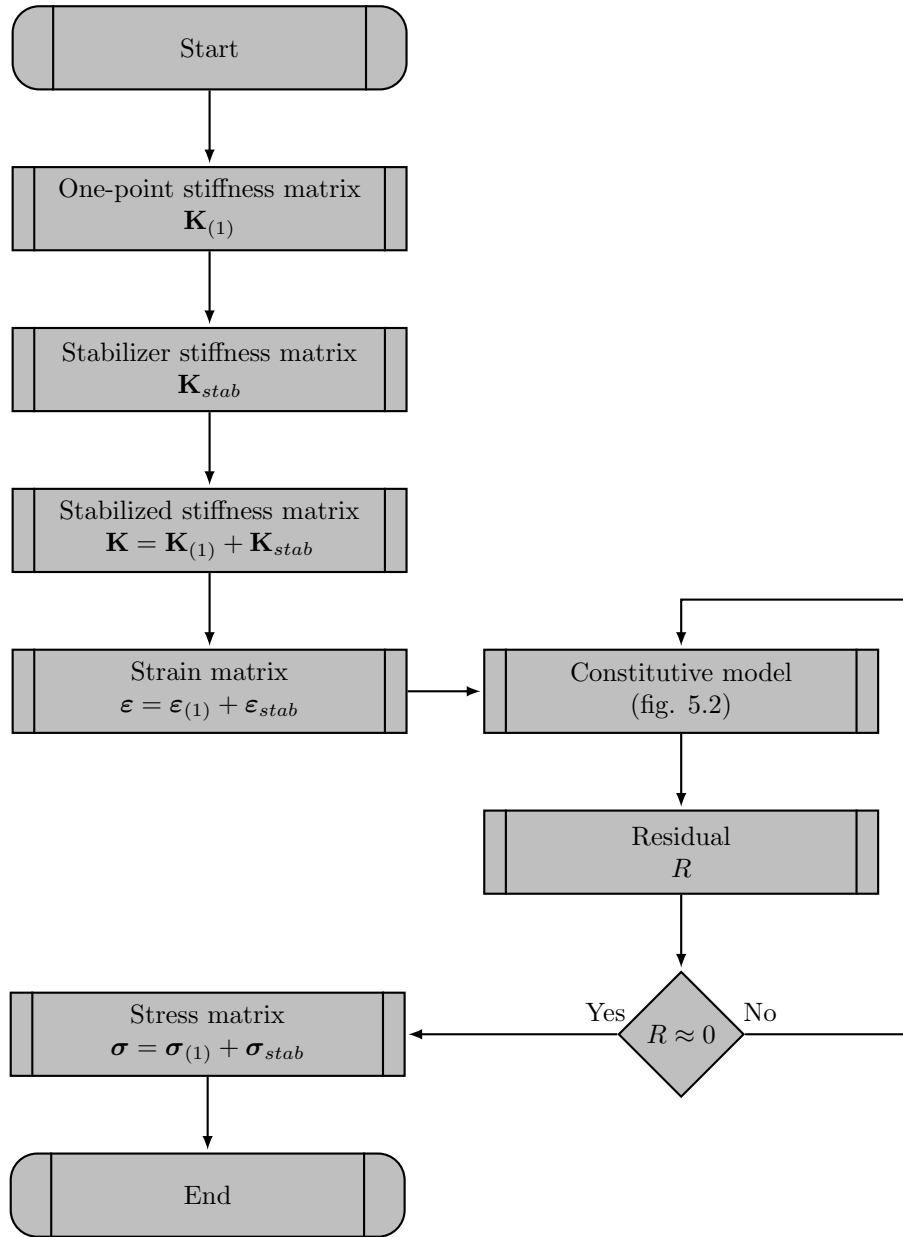


Figure 5.1: *FEAP* (Taylor, 2014) user element routine flowchart

$$A = \frac{1}{2} \left[(x_3 - x_1)(y_4 - y_2) + (x_2 - x_4)(y_3 - y_1) \right] \quad (5.2)$$

$$\mathbf{B}_{(1)} = \frac{1}{2A} \begin{bmatrix} y_{24} & 0 & y_{31} & 0 & y_{42} & 0 & y_{13} & 0 \\ 0 & x_{42} & 0 & x_{13} & 0 & x_{24} & 0 & x_{31} \\ x_{42} & y_{24} & x_{13} & y_{31} & x_{24} & y_{42} & x_{31} & y_{13} \end{bmatrix} \quad (5.3)$$

5.2.2 Stabilizer stiffness matrix

In order to obtain the stabilizer stiffness matrix, \mathbf{K}_{stab} , the hourglass shape vector, γ , must be computed first with eq. 5.4. In this equation \mathbf{b}_x and \mathbf{b}_y are two vectors composed by terms of the one-point compatibility matrix, $\mathbf{B}_{(1)}$ (see eq. 4.21), and $\mathbf{\Gamma}$ is the hourglass base vector from table 4.2.

$$\gamma^T = \frac{1}{4} \left[\mathbf{\Gamma}^T - (\mathbf{\Gamma}^T \mathbf{x}) \mathbf{b}_x^T - (\mathbf{\Gamma}^T \mathbf{y}) \mathbf{b}_y^T \right] \quad (5.4)$$

An algorithm for performing a numerical integration, with a 2 by 2 quadrature, is needed so as to compute the H_{xx} , H_{yy} and H_{xy} terms (eq. 5.5). Here, $h = \xi \eta$ (see eqs. 4.29 and 4.41).

$$H_{xx} = \int_A h_{,x}^2 dA \quad H_{yy} = \int_A h_{,y}^2 dA \quad H_{xy} = \int_A h_{,x} h_{,y} dA \quad (5.5)$$

Once the hourglass shape vector, γ , and the H_{xx} , H_{yy} and H_{xy} terms are calculated, the stabilizer stiffness matrix can be computed with eq. 5.6. It can be noted that each term in this matrix represents a 4-order sub-matrix.

$$\mathbf{K}_{stab} = \left[\begin{array}{c|c} \frac{(c_1 H_{xx} + c_2 H_{yy}) \gamma \gamma^T}{c_3 H_{xy} \gamma \gamma^T} & \frac{c_3 H_{xy} \gamma \gamma^T}{(c_1 H_{yy} + c_2 H_{xx}) \gamma \gamma^T} \end{array} \right] \quad (5.6)$$

The values of the c_1 , c_2 and c_3 constants, for an assumed strain element, are in table 4.3. Since the full procedure for the stabilizer matrix obtaining must be performed in a local-coordinate system, a transformation to the global-coordinate system is needed in order to add this matrix to the one-point stiffness matrix, $\mathbf{K}_{(1)}$. Furthermore, a rearrangement of terms is required for being consistent with the *FEAP* (Taylor, 2014) environment.

It is important to note, that the procedure described above, is analogous to solving eq. 5.7.

$$\mathbf{K}_{stab} = t \int_A \mathbf{B}_{stab}^T \mathbf{C} \mathbf{B}_{stab} dA \quad (5.7)$$

Here, \mathbf{B}_{stab} is the stabilizer compatibility matrix (see eq. 4.38) and can be computed with eq. 5.8.

$$\mathbf{B}_{stab} = \left[\begin{array}{cc|cc|cc|cc} h_{,x} \gamma_1 & 0 & h_{,x} \gamma_2 & 0 & h_{,x} \gamma_3 & 0 & h_{,x} \gamma_4 & 0 \\ 0 & h_{,y} \gamma_1 & 0 & h_{,y} \gamma_2 & 0 & h_{,y} \gamma_3 & 0 & h_{,y} \gamma_4 \\ \hline h_{,x} \gamma_1 & h_{,x} \gamma_1 & h_{,x} \gamma_2 & h_{,x} \gamma_2 & h_{,x} \gamma_3 & h_{,x} \gamma_3 & h_{,x} \gamma_4 & h_{,x} \gamma_4 \end{array} \right] \quad (5.8)$$

5.2.3 Stabilized stiffness matrix

The stabilized stiffness matrix, \mathbf{K} , is obtained by adding the stabilizer stiffness matrix to the one-point stiffness matrix (eq. 5.9).

$$\mathbf{K} = \mathbf{K}_{(1)} + \mathbf{K}_{stab} \quad (5.9)$$

5.2.4 Strain matrix

Once the stabilized stiffness matrix is calculated, the displacements vector, \mathbf{d} , can be obtained by conventional procedures that are already implemented in *FEAP* (Taylor, 2014). For computing the strain matrix, $\boldsymbol{\varepsilon}$, eq. 4.38 is required. It can be seen that in this case the compatibility matrix, \mathbf{B} , is composed by $\mathbf{B}_{(1)} + \mathbf{B}_{stab}$, in order to obtain a stabilized deformations in each integration point for a 4-point quadrature rule (eq. 5.10).

$$\boldsymbol{\varepsilon} = \underbrace{\left[\mathbf{b}_1 \mid \mathbf{b}_2 \mid \mathbf{b}_3 \mid \mathbf{b}_4 \right]}_{\mathbf{B}_{(1)} + \mathbf{B}_{stab}} \mathbf{d} = \boldsymbol{\varepsilon}_{(1)} + \boldsymbol{\varepsilon}_{stab} \quad (5.10)$$

where:

$$\mathbf{b}_i = \begin{bmatrix} b_{xi} + h_{,x} \gamma_i & 0 \\ 0 & b_{yi} + h_{,y} \gamma_i \\ b_{xi} + h_{,x} \gamma_i & b_{xi} + h_{,x} \gamma_i \end{bmatrix} \quad (5.11)$$

5.2.5 Stress matrix

For obtaining the stress matrix, $\boldsymbol{\sigma}$, eq. 5.12 is used. Here, \mathbf{C} is the constitutive matrix.

$$\boldsymbol{\sigma} = \mathbf{C} \boldsymbol{\varepsilon} = \boldsymbol{\sigma}_{(1)} + \boldsymbol{\sigma}_{stab} \quad (5.12)$$

5.2.6 Constitutive model

A return mapping algorithm for plane stress elastoplasticity, developed by Simo and Taylor (1986), is used to simulate a nonlinear material behaviour. This model considers a nonlinear isotropic hardening and the Von Mises yield condition. In fig. 5.2 this algorithm is summarized. Although this constitutive model is not optimal for quasi-fragile structural materials, as the masonry, is useful for the sub-integration scheme validation in nonlinear cases.

It may be important to note that in *FEAP* (Taylor, 2014), the constitutive model is applied to each integration point of a 2 by 2 quadrature, instead of the one integration point of a 1 by 1 quadrature. Then, the constitutive model can be used without modifications.

5.2.7 Residual

The residual must be obtained by the sum of the one-point and four-point stabilizer forces contributions (eq. 5.19).

$$[\mathbf{K}_{(1)} + \mathbf{K}_{stab}] \mathbf{d} = A \mathbf{B}_{(1)}^T \boldsymbol{\sigma}_{(1)} + \int_A \mathbf{B}_{stab}^T \boldsymbol{\sigma}_{stab} dA \quad (5.19)$$

- Update strain tensor. Compute trial elastic stresses

$$\begin{aligned}\boldsymbol{\varepsilon}_{n+1} &= \boldsymbol{\varepsilon}_n + \nabla_s \mathbf{u} \\ \boldsymbol{\sigma}^e &= \mathbf{D} [\boldsymbol{\varepsilon}_{n+1} - \boldsymbol{\varepsilon}_n^p] \\ \boldsymbol{\eta}^e &= \boldsymbol{\sigma}^e - \boldsymbol{\alpha}_n\end{aligned}\quad (5.13)$$

- Consistency at t_{n+1} : Solve $\phi(\lambda) = 0$ for λ

$$\begin{aligned}\phi(\lambda) &:= \frac{1}{2} \bar{\phi}^2(\lambda) - R^2(\lambda) \equiv 0 \\ \bar{\phi}^2 &:= \frac{(\eta_{11}^e - \eta_{22}^e)^2}{2 \left[1 + \left(\frac{E}{3(1-\nu)} + \frac{2}{3} H \right) \lambda \right]^2} + \frac{(\eta_{11}^e - \eta_{22}^e)^2}{2 \left[1 + \left(2G + \frac{2}{3} H \right) \lambda \right]} \\ R^2(\lambda) &:= \frac{1}{3} \kappa^2 \left(\bar{e}_n^p + \alpha \lambda \sqrt{\frac{2}{3}} \bar{\phi}(\lambda) \right)\end{aligned}\quad (5.14)$$

- Compute modified (algorithmic) elastic tangent moduli

$$\boldsymbol{\Xi} = \left[\mathbf{D}^{-1} + \frac{\lambda}{1 + \frac{2}{3} \lambda H} \mathbf{P} \right] \quad (5.15)$$

- Update stresses and plastic strains at t_{n+1}

$$\begin{aligned}\boldsymbol{\eta}_{n+1} &= \frac{1}{1 + \frac{2}{3} \lambda H} \boldsymbol{\Xi}(\lambda) \mathbf{D}^{-1} \boldsymbol{\eta}^e \\ \boldsymbol{\alpha}_{n+1} &= \boldsymbol{\alpha}_n + \lambda \frac{2}{3} H \boldsymbol{\eta}_{n+1} \\ \boldsymbol{\sigma}_{n+1} &= \boldsymbol{\eta}_{n+1} - \boldsymbol{\alpha}_{n+1} \\ \bar{e}_{n+1}^p &= \bar{e}_n^p + \sqrt{\frac{2}{3}} \lambda \bar{\phi}(\lambda) \\ \boldsymbol{\varepsilon}_{n+1}^p &= \boldsymbol{\varepsilon}_n^p + \lambda \mathbf{P} \boldsymbol{\eta}_{n+1}\end{aligned}\quad (5.16)$$

- Compute consistent elastoplastic tangent moduli

$$\begin{aligned}\frac{\partial \boldsymbol{\sigma}}{\partial \boldsymbol{\varepsilon}} \Big|_{n+1} &= \boldsymbol{\Xi} - \frac{[\boldsymbol{\Xi} \mathbf{P} \boldsymbol{\eta}_{n+1}][\boldsymbol{\Xi} \mathbf{P} \boldsymbol{\eta}_{n+1}]^T}{\boldsymbol{\eta}_{n+1}^T \mathbf{P} \boldsymbol{\Xi} \mathbf{P} \boldsymbol{\eta}_{n+1} + \bar{\beta}_{n+1}} \\ \gamma_1 &:= 1 + \frac{2}{3} \mathbf{H} \lambda \quad \gamma_2 := 1 - \frac{2}{3} \kappa'_{n+1} \lambda \\ \bar{\beta}_{n+1} &:= \frac{2}{3} \frac{\gamma_1}{\gamma_2} (\kappa'_{n+1} \gamma_1 + \mathbf{H} \gamma_2) \boldsymbol{\eta}_{n+1}^T \mathbf{P} \boldsymbol{\eta}_{n+1}\end{aligned}\quad (5.17)$$

- Update ε_{33} strain

$$\varepsilon_{33+1} = -\frac{\nu}{E} (\sigma_{11n+1} + \sigma_{22n+1}) - (\varepsilon_{11n+1}^p + \varepsilon_{22n+1}^p) \quad (5.18)$$

Figure 5.2: Return mapping algorithm for plane stress elastoplasticity (Simo and Taylor, 1986)

Validation Examples

6.1 Introduction

In section 4.4, a method for stabilizing a stiffness matrix obtained with reduced integration was validated at level of one single 4-node quadrilateral element. In this chapter, two examples composed by an arrangement of these elements are analyzed, in order to validate both the formulation and the numerical implementation of this procedure for linear and nonlinear cases. Furthermore, a wide discussion of the results is included, focusing in the attractive advantages of this strategy.

As in chapter 3, the problem of the Cook's membrane was selected (Cook, 1974), due to that its analytical solution is known for a linear case. The geometry and restraints are shown in fig. 6.1.

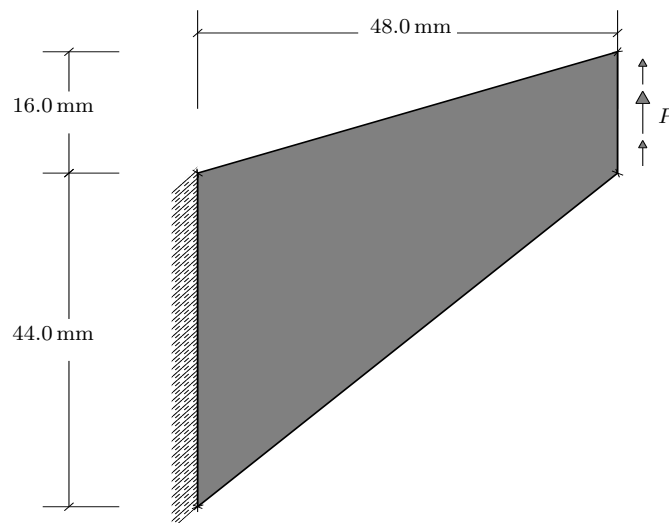


Figure 6.1: Cook's membrane geometry

6.2 Cook's membrane (linear case)

For analyzing the membrane, a Young's module $E = 1,000$ MPa, a Poisson's ratio $\nu = 0.33$ and an applied load $P = 1,000$ N in the free end were considered. This load has a parabolic distribution, as shown in fig. 6.1. Five meshes were built, with 2, 4, 8, 16 and 32 4-node quadrilateral elements at the end where load is applied. A plane-stress problem was analyzed with full and reduced integration, and with the stabilization procedure for different cases of an assumed strain (see table 4.3).

These problems were carried out in *FEAP* (Taylor, 2014), using the implemented algorithm that was described in the former chapter. The characteristic equation of the global stiffness matrix, $(\mathbf{K} - \lambda \mathbf{I})\Phi = \mathbf{0}$, was also solved, in order to perform a comparison among the deformation modes obtained by full and reduced integration with and without stabilization. In figs. 6.2, 6.3 and 6.4 the first three deformation modes of the 16-element mesh are shown. In each figure, there are three sub-figures corresponding to the three cases of numerical integration solved.

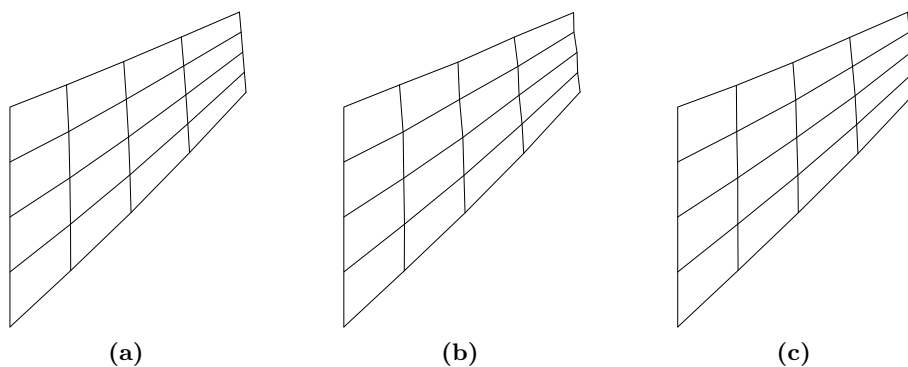


Figure 6.2: Deformation mode 1 of Cook's membrane analyzed with: (a) full, (b) reduced and (c) reduced and stabilized numerical integration scheme

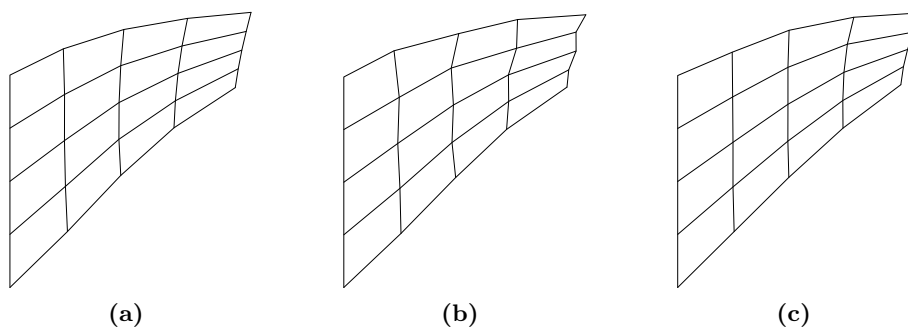


Figure 6.3: Deformation mode 2 of Cook's membrane analyzed with: (a) full, (b) reduced and (c) reduced and stabilized numerical integration scheme

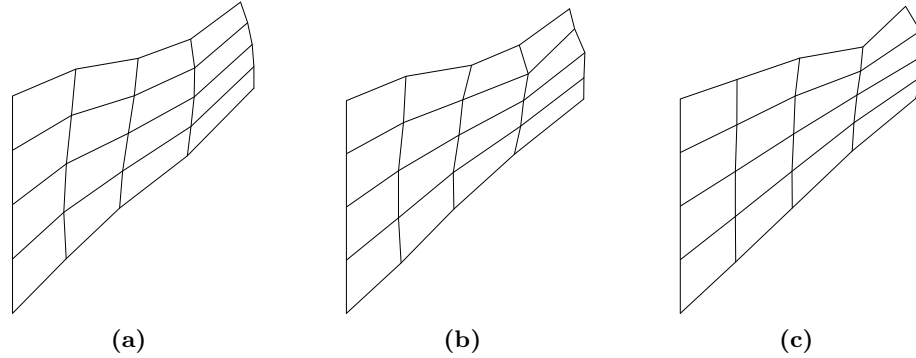


Figure 6.4: Deformation mode 3 of Cook's membrane analyzed with: (a) full, (b) reduced and (c) reduced and stabilized numerical integration scheme

In these graphical representations the same scale factor is used for comparison purposes. Here, it can be noted a quite similar deformed configuration and a clear control of hour-glass effect, which is more evident in the free-end elements of the membrane and along the vertical lines of the mesh.

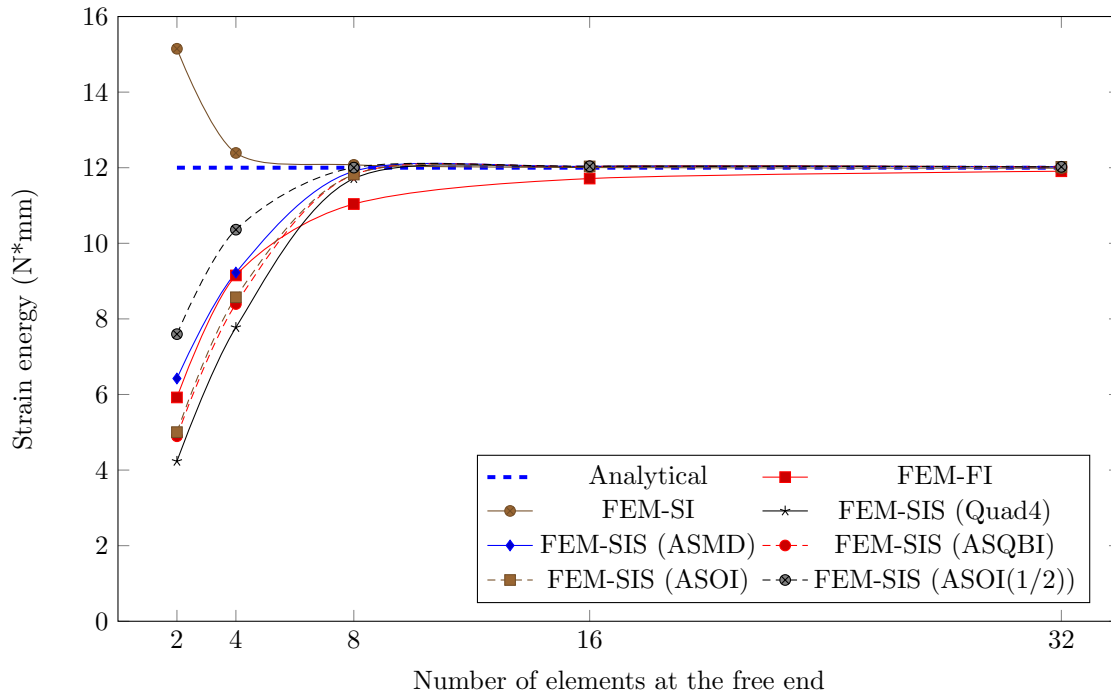
In addition to validate the control of the hourglass effect, a convergence analysis was performed. In fig. 6.5a it can be observed the convergence to the analytical solution of the strain energy, and in fig. 6.5b to the analytical solution of the free-end displacement, for each mesh mentioned above. Here, FEM means finite element method, FI corresponds to a full-integration scheme, SI stands for a sub-integration scheme and SIS for a sub-integration and stabilization scheme. Also, the letters in brackets are for the assumed strain case (see table 4.3).

Several remarks can be done from fig. 6.5. First, a change in the convergence direction is presented when using sub-integration without employing any stabilization procedure. Hence, it can be concluded that while in full-integration the larger the number of elements, the more flexible is the membrane, in reduced integration the opposite occurs. Second, when applying the stabilization procedure, the convergence direction is the same as in full-integration. Third, an acceptable solution is reached with fewer elements in comparison with full-integration, even when the most deficient assumed-strain scheme is applied.

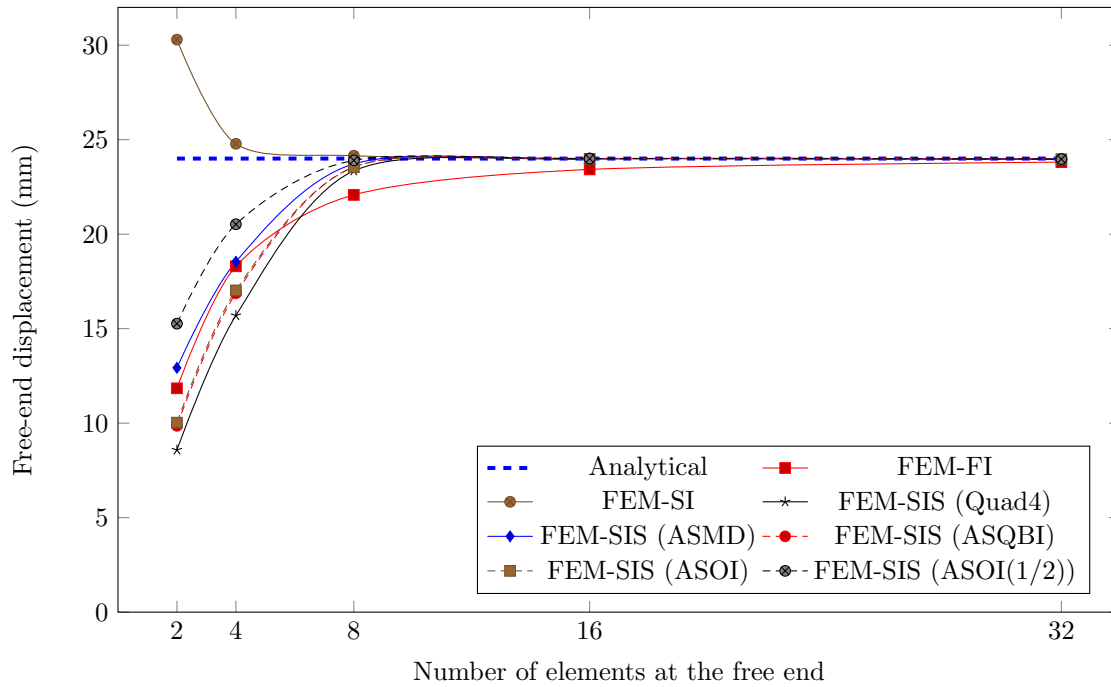
These remarks imply that the stabilization procedure is not only faster in computing-time terms for a mesh-to-mesh comparison, besides it is more accurate and it need coarser meshes for a good-enough approximation, which means an even greater computational cost reduction.

Forasmuch these results, the formulation and the numerical implementation are validated for linear cases. In spite of that the advantages studied in this example are clearly attractive, they are so much more attractive for nonlinear cases, especially when the problem involves large computation volumes, as in structural analysis of ancient masonry constructions.

6. VALIDATION EXAMPLES



(a)



(b)

Figure 6.5: Cook's membrane convergence to analytical solution in (a) strain energy and (b) free-end displacement

6.3 Cook's membrane (nonlinear case)

To validate the algorithm implemented in *FEAP* (Taylor, 2014) for nonlinear cases, a problem with the same Cook's membrane is proposed. Instead of loads, displacements were imposed in the free end, in order to avoid convergence troubles. Two meshes, termed *A* and *B*, were selected from the five used in the linear case in the former section. The *A* mesh is composed by 64 4-node quadrilateral elements, while the *B* has 1,024. These meshes are shown in fig. 6.6.

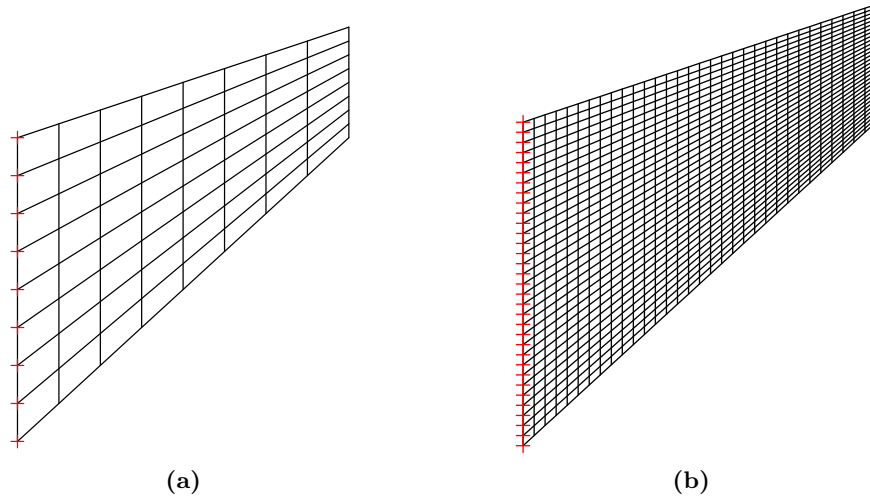


Figure 6.6: Cook's membrane (a) *A* mesh and (b) *B* mesh

For analyzing the plane-stress problem, the next mechanical properties for the material were considered: a Young's module $E = 2,000$ MPa, a Poisson's ratio $\nu = 0.20$, a yield stress $Y_0 = 50$ MPa and a hardening variable $H = 1$.

The nonlinear behaviour was simulated using the return mapping algorithm from fig. 5.2 (Simo and Taylor, 1986). The mathematical nonlinear problem was approximated by applying the modified Newton-Raphson method, imposing a 5 mm displacement in 200 steps.

Both meshes were analyzed with full and reduced numerical integration with the stabilization procedure. Figure 6.7 shows the zones in which the yield stress is reached with the Von Mises criterion. It can be noted that the stresses distributions of the Cook's membrane are similar for both cases. An interesting remark of this comparison, is that the stress distribution in the *A* mesh solved with reduced integration is more similar to the ones in the *B* mesh.

In fig. 6.8 reaction-displacement curves are shown, in order to validate in a more representative way the general behaviour of the membrane. Several remarks can be done from this figure. First, the results between both types of numerical integration are very similar.

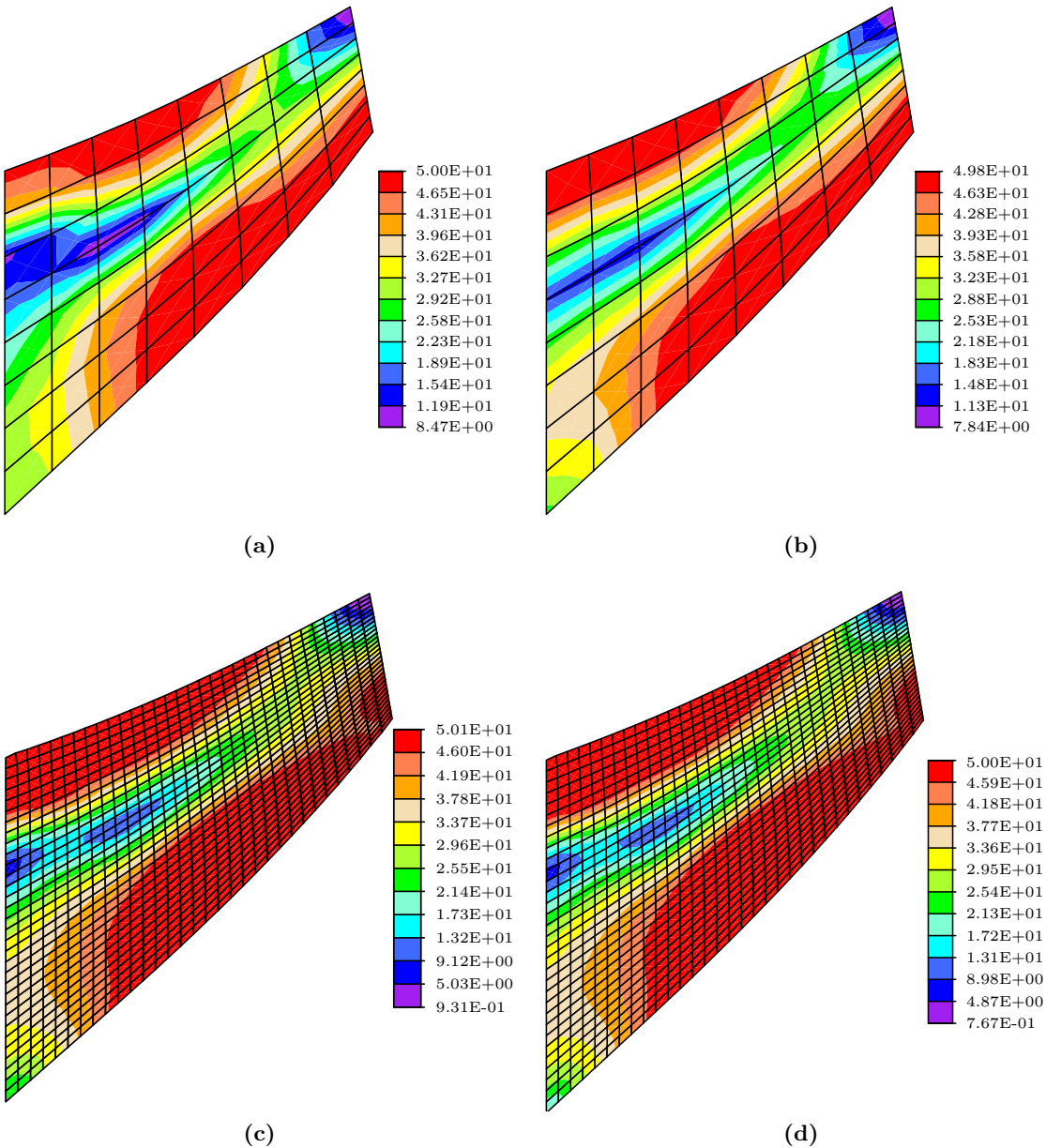


Figure 6.7: Von Mises stress distribution of Cook's membrane analyzed with A mesh by (a) sub-integration and (b) full-integration; and B mesh by (c) sub-integration and (d) full-integration

Second, the similitude in a mesh-to-mesh comparison is better when the mesh has more elements. Third, the behaviour approximated with the A mesh using reduced integration is closer to the ones reached with the B mesh. The highest difference between these two results is 2.96%.

This last remark is the most attractive advantage for using reduced numerical integration

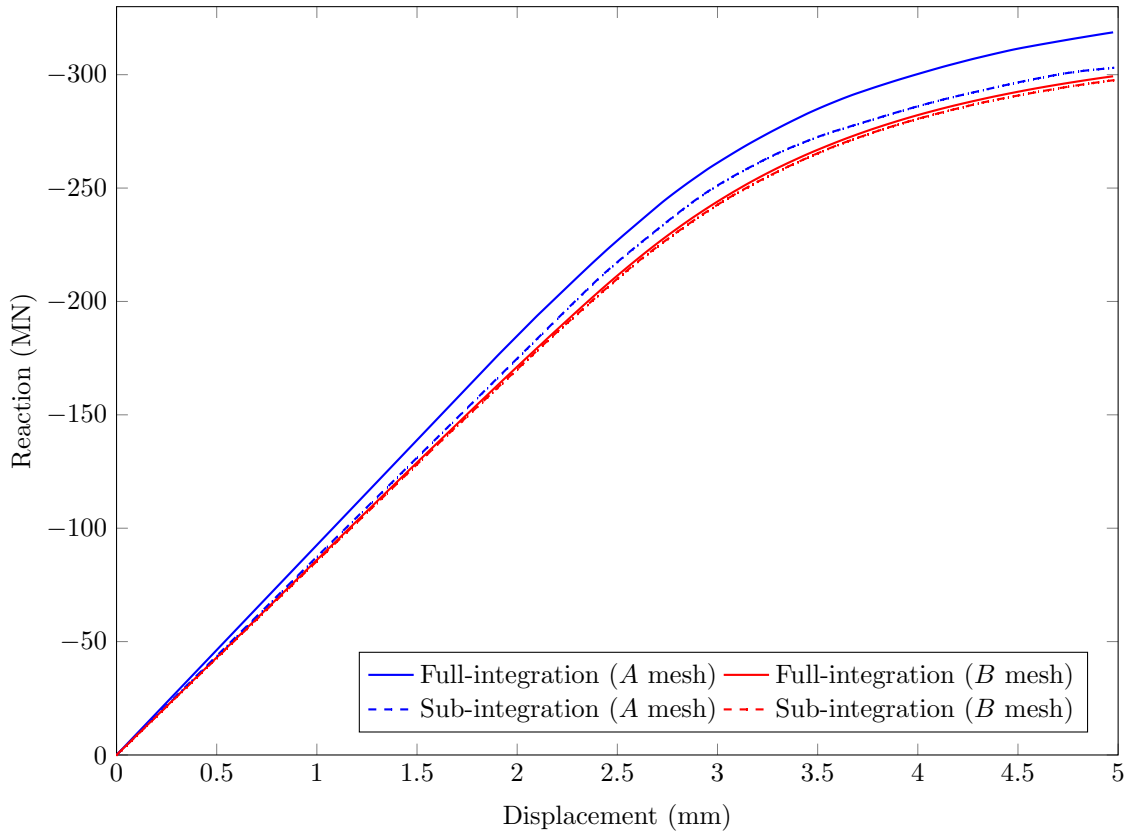


Figure 6.8: Cook's membrane reaction-displacement diagram

in the approximation of nonlinear problems. Since the computational cost for analyzing this type of problems is proportional to the number of elements composing the mesh, the analysis is much faster. In this case, the computing-time reduction is 40.73%. The main impact of this computational cost reduction, is the possibility of employing more sophisticated constitutive models for the practical engineering analysis, and not only in research works.

In spite of that the real solution of the nonlinear problem is unknown, it is known that a finite element approximation is closer to the solution when the number of elements is higher. So, a comparison between the results with both schemes of numerical integration should be enough to validate the algorithm.

Application Examples

7.1 Introduction

In order to apply the sub-integration scheme with hourglass control studied and validated in the former chapters, two examples of historical masonry buildings are analyzed. The first one corresponds to a shear wall that represents a typical house facade. The second one is a section of the monastery of São Vicente de Fora, which is a very important historic monument in Lisbon, Portugal.

Both problems were solved with nonlinear material behaviour through full and reduced numerical integration, employing two meshes with different number of elements. A comparison among the results of yield stresses distribution is included. Also, reaction-displacement curves are incorporated, so the structural behaviour of the building can be compared.

Interesting remarks are presented in a final section of the chapter, focusing in the advantages and drawbacks of using reduced integration for analyzing nonlinear problems.

7.2 Shear wall with openings

A shear wall with two door openings, tested by Bono et al. (1998) and studied by Orduña (2003) with rigid block models, was selected for applying the sub-integration scheme studied in this thesis. The wall is 5.80 m long and 3.60 m high. The dimensions of the two doors openings are 1.0x2.20 m. The masonry has a Young's module $E = 1,750$ MPa, a Poisson's ratio $\nu = 0.20$ and a yield stress $Y_0 = 3.50$ MPa. All these mechanical properties were selected from the standards of the *Complementary technical standards of the Construction code for the Federal District* (GDF, 2004).

Two meshes were elaborated, termed *A* and *B* mesh, with 1,284 and 5,140 4-node quadrilateral elements respectively (fig. 7.1). The problem was analyzed using the *FEAP* (Taylor, 2014) program. The modified Newton-Raphson method was employed for approximating the nonlinear mathematical problem. Displacements of 5 cm were imposed in 200 steps, in the top-wall elements.

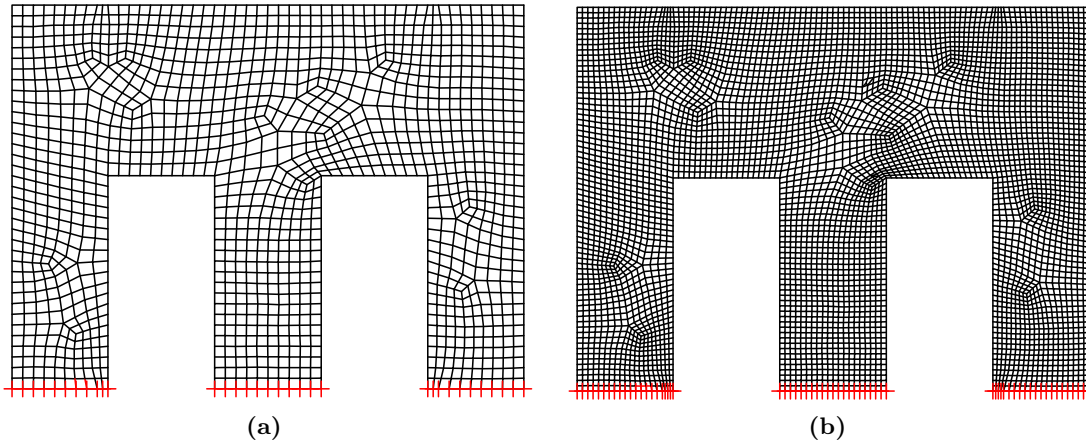


Figure 7.1: Shear wall with openings (a) *A* mesh and (b) *B* mesh

Reaction-displacement curves are included in fig. 7.2. The maximum difference between both numerical integration cases for the *A* mesh is 1.57%, and for the *B* mesh is 0.79%. An interesting fact is that, as expected, the computation time of solving the problem with reduced integration is lower than with full integration.

Although the curve for the *A* mesh with reduced integration is slightly more similar to the *B* mesh curve, for this particular problem both meshes have similar behaviour, regardless the order of quadrature used.

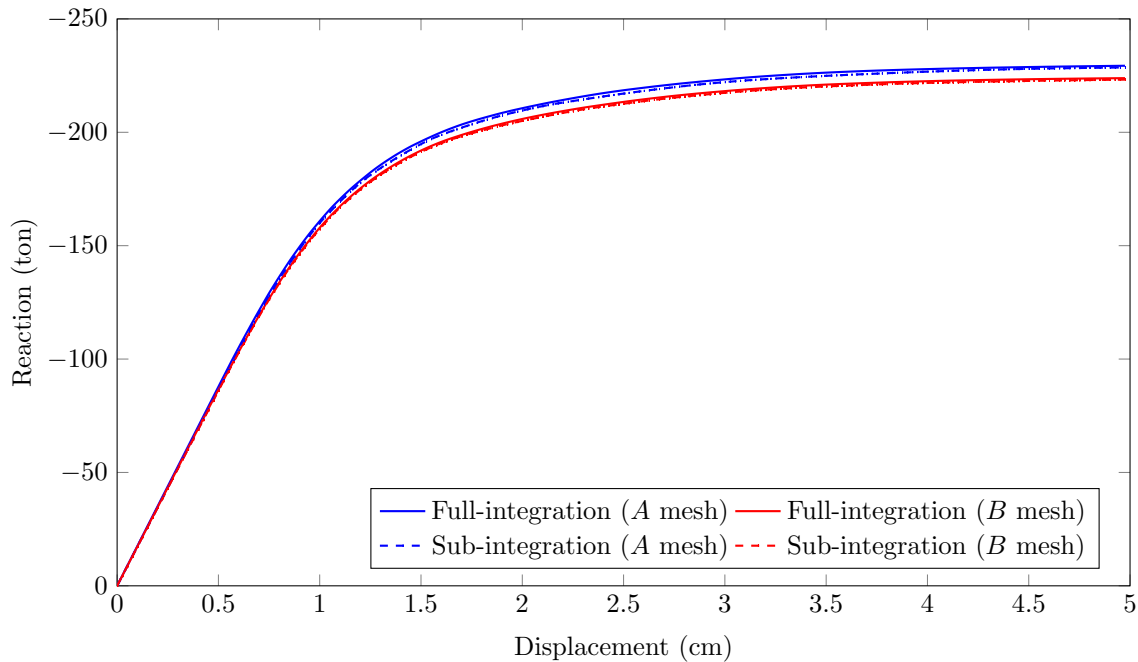
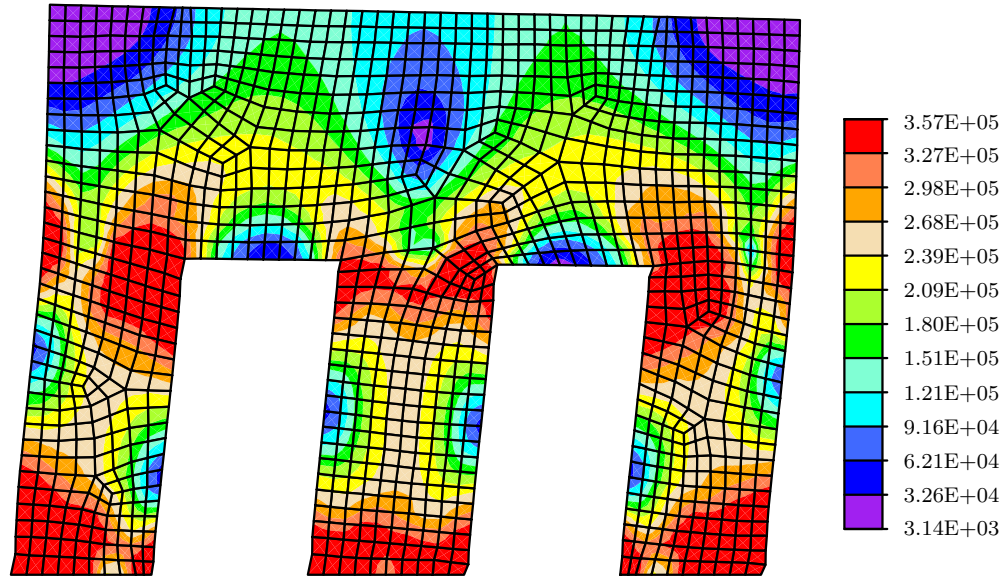
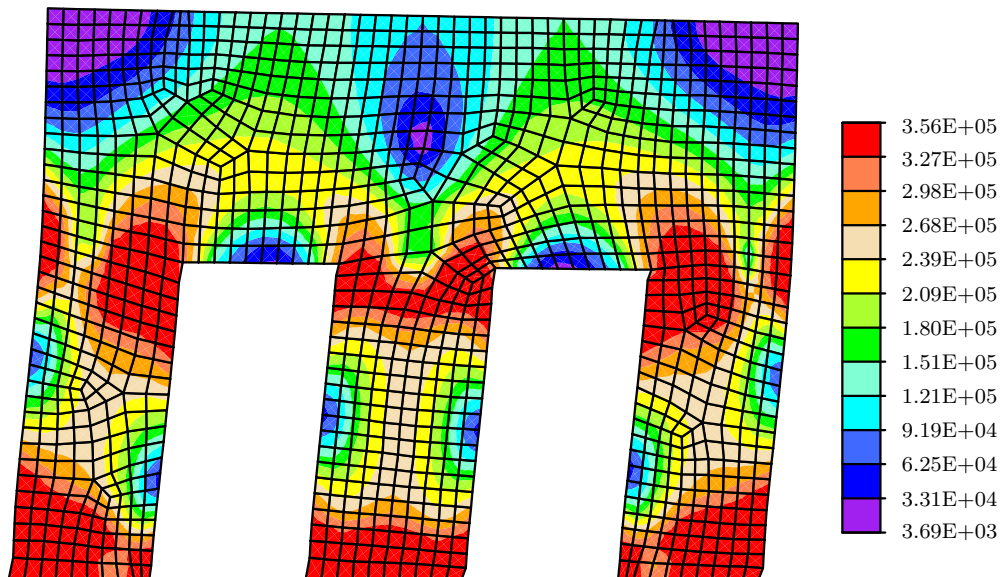


Figure 7.2: Shear wall with openings displacement-reaction diagram

In this problem, the linear-strain or flexural modes have an insignificant contribution to the global behaviour of the wall. This is the reason for the high similarity between both numerical integration schemes. In other cases, in which the flexural modes are more participative, the results with reduced integration are better in comparison to full integration ones. As in the Cook's membrane problem studied in the former chapter.

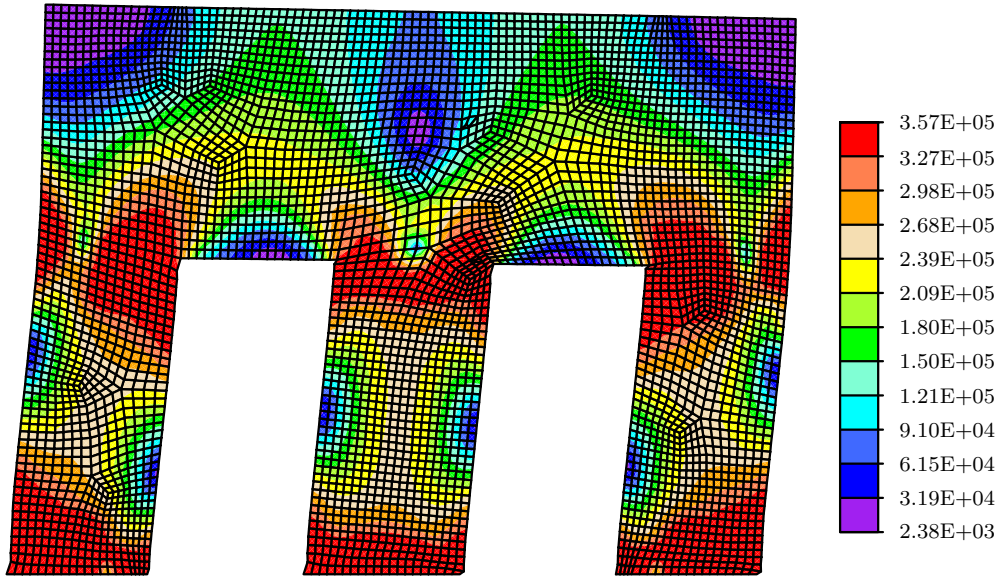


(a)

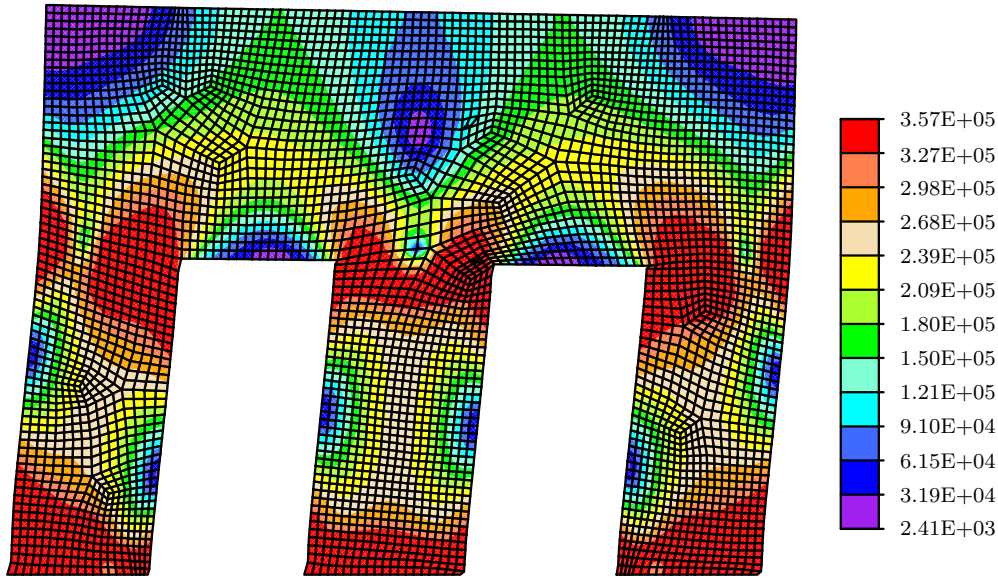


(b)

Figure 7.3: Von Mises stress distribution of shear wall with openings analyzed with A mesh by (a) reduced and (b) full numerical integration



(a)



(b)

Figure 7.4: Von Mises stress distribution of shear wall with openings analyzed with B mesh by (a) reduced and (b) full numerical integration

In figs. 7.3 and 7.4, the Von Mises yield stresses distribution is shown for both cases of numerical integration and the analyzed meshes. A clear similarity can be seen among all the cases.

7.3 Monastery of São Vicente de Fora

Another selected application example is the arcade of the monastery of São Vicente de Fora (see fig. 2.1a). This monastery, founded in 1147 by D. Alfonso Henriques, was built on one of the east hills of the city of Lisbon, in Portugal. The Lisbon earthquake of 1755 caused very serious damage to the church and the monastery (Correia et al., 2007). Because of the history behind this building and its architectural beauty, there is a high interest in preserving it.

The main structure is conformed by columns and arches of stone blocks joined with mortar. In the ELSA Laboratory, many experiments were performed on a real-scale model of one section of the monastery that includes three columns, two arches and two semi-arches (Correia et al., 2007; Pegon et al., 2001). In fig. 7.5 a photograph of the model is included.

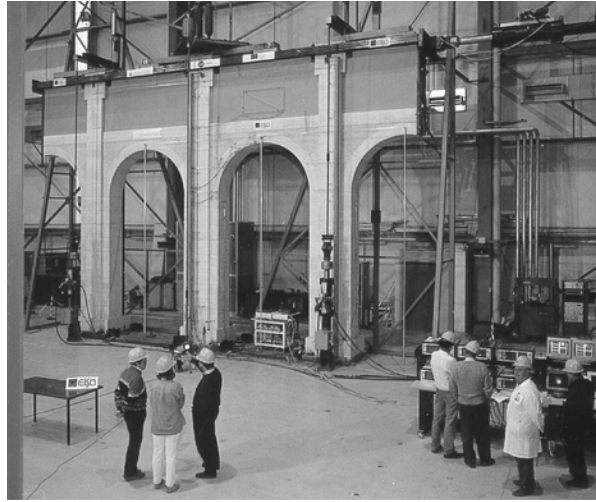


Figure 7.5: Full-scale model at the ELSA Laboratory (Pegon et al., 2001)

Several researchers used the results of these experiments in order to validate or apply numerical models proposed for simulating the masonry behaviour as structural material, for example Meza et al. (2008) and Orduña et al. (2004b). In this work, no experimental results are used, because the main objective is to validate the reduced numerical integration scheme. In future works, a constitutive model of plasticity and damage for masonry will be proposed and applied with this scheme of sub-integration.

The geometry used for the analysis is consistent with the full-scale model (fig. 7.5). The model is 7.45 m high and 10.80 m long. The three columns have 0.80 m width and are spaced at each 3.60 m. The arches are 1.25 m high. The masonry has a Young's module $E = 1,000$ MPa, a Poisson's ratio $\nu = 0.20$ and a yield stress $Y_0 = 100$ kPa. All these mechanical properties were selected according to the experiment reports, summarized by Meza et al. (2008).

Two meshes, termed *A* and *B*, were used in order to show the advantages of using the

7. APPLICATION EXAMPLES

reduced numerical integration scheme studied. Both meshes were elaborated only with 4-node quadrilateral elements. While the *A* mesh is composed by 1,323 elements, the *B* mesh has 5,352 (fig. 7.6).

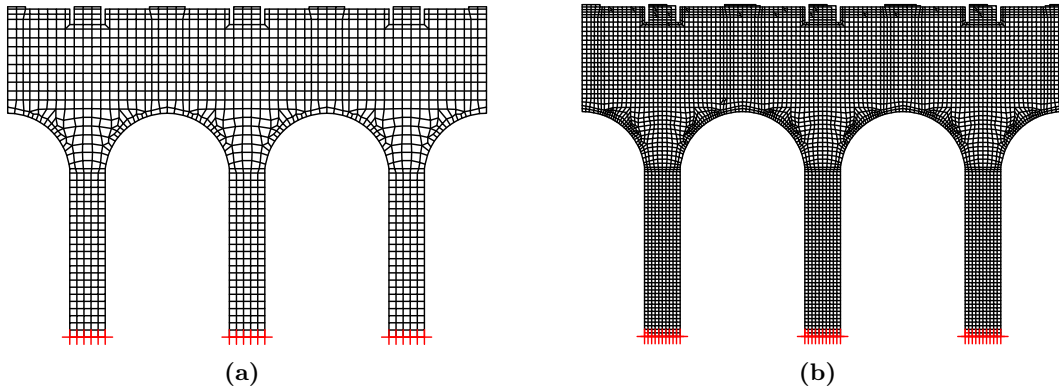


Figure 7.6: Arcade of monastery of São Vicente de Fora (a) *A* mesh and (b) *B* mesh

The problem was analyzed using full and reduced integration in the *FEAP* (Taylor, 2014) program. The modified Newton-Raphson method was employed for approximating the nonlinear mathematical problem. Displacements of 5 cm were imposed in 200 steps, in the top-arcade elements. Reaction-displacement curves are included in fig. 7.7.

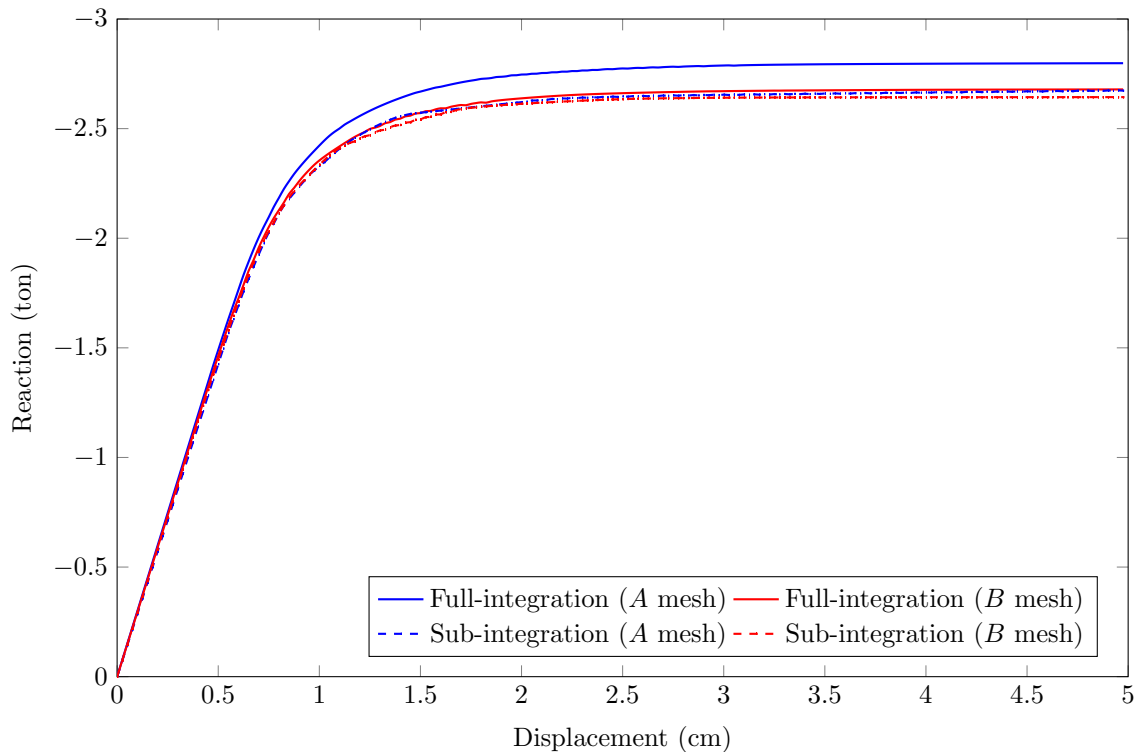
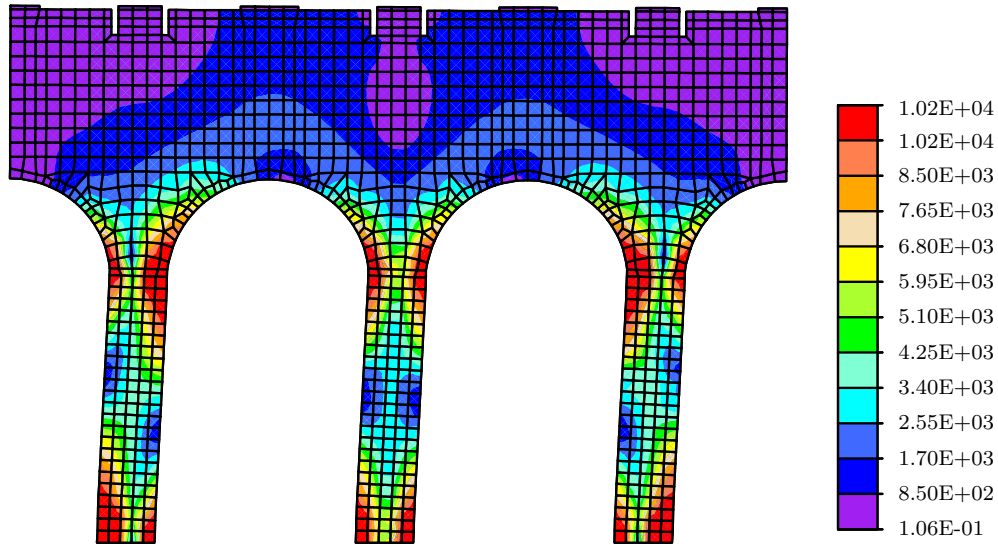
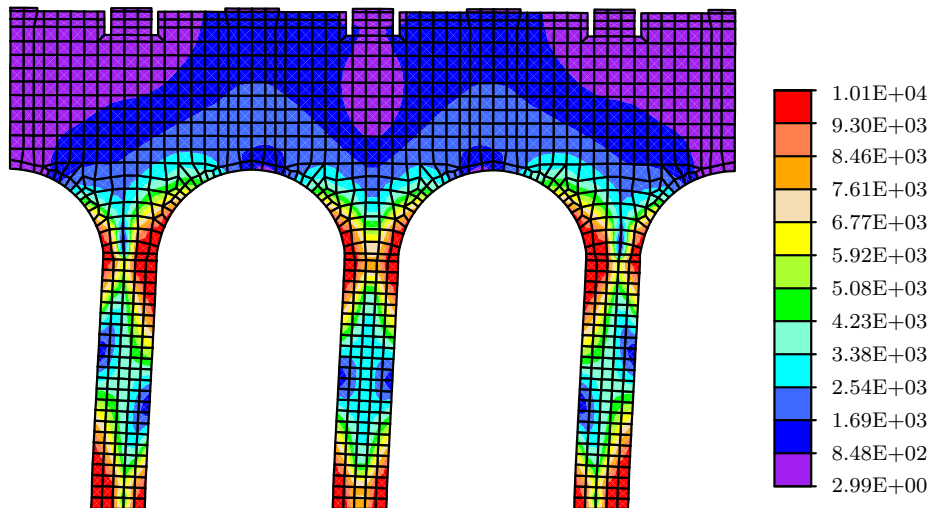


Figure 7.7: Arcade of monastery of São Vicente de Fora displacement-reaction diagram

Several remarks can be done from fig. 7.7. First, the results are very similar between both types of numerical integration for the B mesh analysis. Second, the similitude in a mesh-to-mesh comparison is better when the mesh has more elements. Third, the behaviour approximated with the A mesh by reduced integration is closer to the ones reached with the B mesh. The maximum difference between these two results is 3.04 %, and the average difference is 0.80 %.



(a)



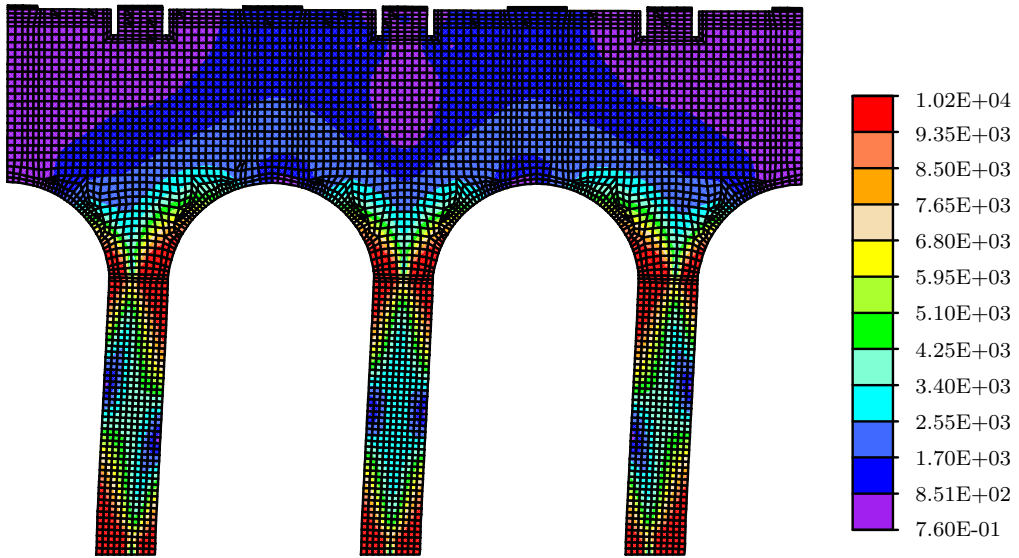
(b)

Figure 7.8: Von Mises stress distribution of the arcade of monastery of São Vicente de Fora analyzed with A mesh by (a) reduced and (b) complete numerical integration

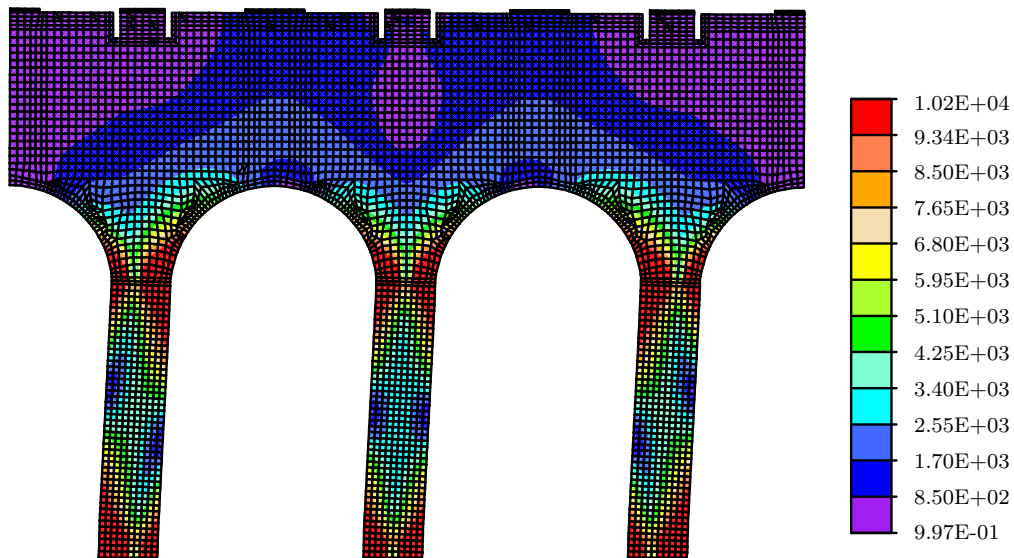
As mentioned in the former chapter, this last remark is the most attractive advantage for using reduced numerical integration in the approximation of nonlinear problems. In this

7. APPLICATION EXAMPLES

case, the reduction in computing time is 73.65%. It means that when the problem involves a larger computation time, the computational cost reduction is higher, which makes its application more attractive.



(a)



(b)

Figure 7.9: Von Mises stress distribution of the arcade of monastery of São Vicente de Fora analyzed with B mesh by (a) reduced and (b) complete numerical integration

In figs. 7.8 and 7.9, a Von Mises yield stresses distribution is showed for both cases of

numerical integration and both meshes. A clear similarity is noted among all the cases, especially when the yield stress is reached.

7.4 Discussion of results

Although the Von Mises yield criterion is not optimal for quasi-fragile materials as masonry, the main objective of these application examples is to demonstrate that the sub-integration scheme, studied and applied, successfully reduces the computational cost in nonlinear analysis. Also, the results obtained justify the development of a sophisticated constitutive model of plasticity and damage optimal for masonry, as a future work.

It was proved that this strategy gives high-accuracy results with large reduction in computing time, and also allows the use of coarse meshes. Although the use of this type of meshes is sensitive to the mesh configuration, since the strain-energy contribution of the flexural modes needs to be significant, the sub-integration scheme is faster in a mesh-to-mesh comparison. Thereby, the computational cost reduction is guaranteed regardless the mesh employed.

Finally, in these two application examples, was demonstrated that the sub-integration scheme with hourglass control was correctly implemented in *FEAP* (Taylor, 2014), and it is applicable to any two-dimensional problem for research purposes. Furthermore, several finite element developments can be implemented within this strategy, leading to novel, economical and highly-accurate applications in different research areas of the structural analysis.

Comments and Conclusions

In this dissertation, an alternative strategy for the computational cost reduction in the structural analysis of ancient masonry constructions is studied. This strategy is based in the use of reduced numerical integration rules within the finite element method. The main objective of this research was successfully accomplished, since the resulting implementation is an improved finite element model, which reduces the computational cost of performing a structural analysis. An important remark is that this reduction is reached by focusing in the achievement of high-accuracy results with coarse meshes, instead of poor approximations with fine meshes.

Chapter 3 of this thesis is devoted to the rigid block models. The formulation of these models was reviewed and applied to one example. The major advantage of this strategy is, under certain circumstances, the computational cost reduction, due to the condensation of degrees of freedom in one rigid block, which can be a macro-block that contains a portion of masonry with similar behaviour. In spite of the drawbacks, which were found in chapter 3, this method is useful in practical engineering, where the high-accuracy results can be non essential in order to reach a faster decision making process. This is why these rigid block models are aimed to the structural assessment of large ancient masonry buildings.

A sub-integration scheme with hourglass control for the 4-node quadrilateral finite element was widely studied and applied. In a first step, the method was reviewed at level of one single element, focusing in the mathematical issues generated for applying a reduced numerical integration, as the rank-deficient stiffness matrix. This formulation correctly augments the rank of the one-point stiffness matrix, controls the zero-energy modes and represents better the linear-strain or flexural modes. Also, it is computationally economic, since no large computations are required for its application.

Its numerical implementation was successfully coded in the *FEAP* (Taylor, 2014) program. The routine and subroutines created were computationally optimized and adapted to the software environment, in order to take full advantage of the method. The main impact of this implementation is the possibility of employing it in any two-dimensional finite element model, for research purposes.

Validation and application examples were included along the last chapters. In these exam-

ples, interesting advantages were reviewed. The most attractive one, is the possibility of using high coarse meshes in finite element analysis, which means an even higher reduction of computational cost, especially for nonlinear cases. One reason of this phenomenon, is the improvement in the representation and the strain-energy contribution of the flexural deformation modes. It was demonstrated that, when this energy contribution is considerable, the results with the sub-integration scheme are better than with full-integration, and if this energy contribution is insignificant, both results are highly similar. Thereby, in the worst case, the results obtained with the scheme studied are the same than the ones computed with conventional full integration.

The results obtained in the two nonlinear application examples are highly remarkable. A considerable computational cost was achieved in comparison to the full-integration conventional procedure. This computing-time reduction allows the possibility for developing future works with this sub-integration scheme.

8.1 Future works

As mentioned before, the results of this thesis justify the interest in development of future works, in the area of structural analysis of massive masonry structures. In the following paragraphs, a brief description of many suggested works is included.

Reduction of computational cost allows the development of more sophisticated constitutive models, which simulate better the behaviour of the masonry as structural material. Constitutive models of plasticity and damage are optimal for quasi-fragile materials, as masonry. Also, it is important to consider the mechanical characteristics of this orthotropic material, for instance its almost null tensile strength which leads to nonlinear behaviour beginning with small loads, and its softening phenomenon characteristic of the quasi-fragile materials. A constitutive model with this features, implemented with the sub-integration scheme studied in this thesis, will lead to a full strategy for the optimal study of massive masonry structures.

The dynamic analysis of this type of structures involves large computational cost. Accordingly, the use of the sub-integration scheme becomes in a very attractive alternative for these cases. This research topic is important, since the seismic events generate the most critical damage to a masonry structure, thereby a dynamic analysis is required so as to guarantees the structural safety of the construction.

For applying the reduced integration scheme in the practical engineering, the extrapolation of it, to three-dimensional cases, is a necessary requirement. Although, for research purposes, the two-dimensional cases should be enough for obtaining successful results in the study of a problem, in the labor field of structural engineering three-dimensional analysis are necessary for performing a realistic study of the building. Also, in these cases the computational cost reduction should be higher.

In this thesis and in these suggested works, the focused structural material is the masonry.

Nevertheless, this sub-integration scheme is, obviously, applicable to any other structural materials. So, several developments and novel applications can be carried out with this sub-integration scheme to many areas of structural engineering, especially when large computations are involved.

The Framework Method

A.1 Introduction

In this appendix, a theoretical overview of many numerical methods is included, in order to contextualize the evolution of the investigated in this thesis. The formulation of the framework method, developed by Hrennikoff (1949), is reviewed and applied to one example with known solution. The results in convergence to strain energy are discussed. Also, the eigen-analysis of the model is performed and the resulting deformation modes are compared to those obtained with the finite element method. Finally, several remarks are presented.

A.2 Numerical methods

Numerical methods, as distinct from *analytical* methods, deal with the numerical values of the significant variables at all stages of the computation. Variations in material properties and boundary conditions that are often impossible to consider by formal methods may usually be considered quite readily by the cruder but more adaptable and flexible numerical methods. In many respects numerical procedures are like experiments: to find a functional relationship, for example, one may have to solve a series of problems and examine or plot the results (Newmark, 1949).

Numerical methods may in general be divided into several types, and obvious distinction can be made between those based on mathematical concepts and those based on physical action or analogy. From the mathematical point of view are the *iterative methods* and *step-by-step methods*. From the physical standpoint a classification can be set up in terms of the methods and concepts of stress analysis of a structure: *relaxation*, *continuity restoration* and *trial loads* (Newmark, 1949).

A distinction must be made between those methods which involve operations on elements, and those which involve operations on the whole. The methods described before are all of the former type. The latter type include methods such as energy methods and procedures involving the minimization of certain error functions leading to a set of algebraic

equations. Important examples of such *variational* methods, in addition to the methods of minimum potential energy, and the method of minimum complementary energy, are: *collocation*, *least squares*, *weighted least squares* and *Galerkin's method*. These methods not necessarily involve numerical procedures, but they can be used numerically as they can often be related to the more direct numerical processes (Newmark, 1949).

In general terms there are two types of problems that can be solved by numerical methods: *discrete joint problems* and *continuum problems*. The first ones are problems that have a finite number of degrees of freedom, where values of a significant variable are to be determined only at discrete points or *joints*. The solution of these problems has a counterpart in terms of a set of simultaneous algebraic equations which may or may not be linear. On the other hand, the continuum problems are problems in which a variable is to be determined over a whole region generally involve differential or integral equations which may or may not be linear (Newmark, 1949).

In general, the ordinary numerical methods are adaptable only to discrete joint problems, and the variational methods to continuum problems. However, numerical methods may often be used in variational procedures. Two principal techniques are available for the application of the ordinary numerical methods to continuum problems (Newmark, 1949):

- *Mathematically*, by the substitution of finite differences for derivatives, or in general, by the approximation of the continuum problem with a discrete joint or nodal system.
- *Physically*, by a lattice, framework, or other structural or mechanical model. This physical analogy to the actual problem is not an exact one, but it may be made as accurate as desired except where discontinuities or singularities are involved.

The two techniques are related; it is often possible to develop a mechanical model for which the exact solution leads to the same equations that are obtained by means of a finite difference procedure applied to the continuum (Newmark, 1949).

A.3 Formulation

Hrennikoff (1949), developed the *Framework Method*. The basic idea of this method consists on replacing the continuous material of the elastic bodies under investigation by a framework of bars, arranged according to a definite pattern, whose elements are endowed with elastic properties suitable to the type of problem. The criterion of suitability of the framework pattern is equality in deformability of the framework and the solid material in elasticity (Kotronis et al., 2003).

When the units are infinitesimal the framework of this kind is rigorously equivalent to the prototype with regard to the stresses and deformations. Otherwise, when the units are finite, the framework method is not exact, but it still gives a close approximation. Size of the unit is arbitrary, as long as it fits the shape of the prototype. The smaller the unit the more laborious the solution, but the results are closer to reality (Hrennikoff, 1949).

The pattern in the bars of the framework is not arbitrary, although it is not unique. In order to reproduce the faithfully the behaviour of the plate, the framework must have the same deformability as the plate. This statement is the criterion of equivalence of the framework and the plate; it may be conveniently stated in terms of the following three conditions (Hrennikoff, 1949):

1. The framework is loaded uniformly with the normal load p per unit length on the X plane and νp on the Y plane. The normal unit strains in the framework ε_x and ε_y are expressed in terms of the frameworks characteristics and they are equated to the corresponding strains in the plate, loaded with the same loads. These equations are as follows:

$$\varepsilon_x = \frac{p(1 - \nu^2)}{Et} \tag{A.1a}$$

$$\varepsilon_y = 0 \tag{A.1b}$$

2. Reversing the planes X and Y , on which the normal loads p and νp are applied, two similar equations are set up:

$$\varepsilon_x = 0 \tag{A.2a}$$

$$\varepsilon_y = \frac{p(1 - \nu^2)}{Et} \tag{A.2b}$$

3. A uniform tangential load p per unit length is applied, both of the X and Y planes, and the resultant unit shear deformation of the framework is:

$$\gamma_{xy} = \frac{2(1 + \nu)p}{Et} \tag{A.3}$$

Several patterns of the framework have been found valid, and the most convenient of them is the square pattern represented in fig. A.1a, and consisting of squares of size a by a , containing interior squares of the size $\frac{1}{2}a$ by $\frac{1}{2}a$. Three kinds of bars enter construction of each cell (Hrennikoff, 1949):

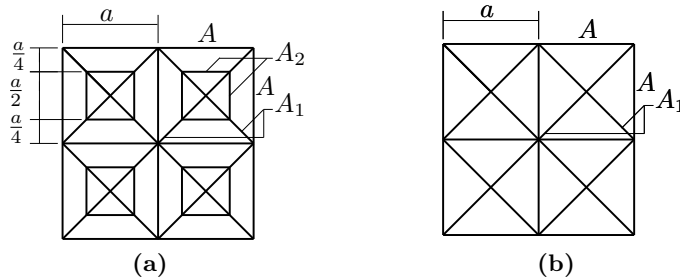


Figure A.1: Square pattern of framework for (a) $\nu \neq \frac{1}{3}$ (b) $\nu = \frac{1}{3}$

- Bars lying along the sides of the main squares, except those coinciding with the periphery of the plate, each have the cross sectional area of eq. A.4. Here t and ν are the thickness and the Poisson's ratio of the plate prototype. Marginal bars have their areas only half as large as the areas A in eq. A.4.

$$A = \frac{at}{1 + \nu} \quad (\text{A.4})$$

- Diagonal bars have on their whole lengths the cross-section area A_1 (eq. A.5), and secondary bars of the length $\frac{1}{2}a$ inside the squares have the area A_2 (eq. A.6).

$$A_1 = \frac{at}{\sqrt{2}(1 + \nu)} \quad (\text{A.5})$$

$$A_2 = \frac{(3\nu - 1)}{2(1 + \nu)(1 - 2\nu)}at \quad (\text{A.6})$$

The areas A , A_1 and A_2 are the functions of the Poisson's ratio ν . For $\nu = 1/3$ the area A_2 become zero, and the pattern reduces to the simple square type shown in figure A.1b, with the areas (Hrennikoff, 1949):

$$A = \frac{3}{4}at \quad (\text{A.7})$$

$$A_1 = \frac{3}{4\sqrt{2}}at \quad (\text{A.8})$$

The most practicable method of analysis of the square framework is an adaptation of the method of joint displacements. If the elastic displacements of the joints are found, and the joints are brought into their true displaced positions, the bar stresses and the external forces acting at each joint are mutually balanced. Instead of finding these displacements from equations, it is possible to guess them roughly on the basis of the applied loads, displace the joints one by one by the amounts guessed, compute the bar stresses caused by these displacements and then determinate the remaining unbalanced joint forces. This operation is repeated many times until a close balance is established at all joints (Hrennikoff, 1949).

Applying the formulation described above, for a unit cell in which $\nu = 1/3$ (fig. A.1b), the stiffness matrix, $\mathbf{K}_{A_2=0}$, is obtained with the resulting eq. A.9. Here, $\alpha_1 = (\sqrt{3} + 3)$ and $\alpha_2 = (\sqrt{3} + 6)$. It can be noted that if $A_2 = 0$ the number of degrees of freedom decreases to eight, two per node as in a 4-node quadrilateral finite element. So, a stiffness matrix for a unit cell in which $\nu \neq 1/3$ (fig. A.1a), has eight extra degrees of freedom, because $A_2 \neq 0$ and consequently the number of nodes are augmented to eight. Hence, the reason for using $\nu = 1/3$ is to compare, in the following application example, the deformation modes of this formulation with the ones obtained with finite element method.

$$\mathbf{K}_{A_2=0} = \frac{E}{16} \begin{bmatrix} 2\alpha_1 & 0 & -6 & 0 & -\sqrt{3} & -\sqrt{3} & -\sqrt{3} & \sqrt{3} \\ 0 & 2\alpha_1 & 0 & 0 & -\sqrt{3} & -\sqrt{3} & \sqrt{3} & 2\alpha_2 \\ -6 & 0 & 6 & 0 & 0 & 0 & 0 & 0 \\ 0 & 0 & 0 & 6 & 0 & -6 & 0 & 0 \\ -\sqrt{3} & -\sqrt{3} & 0 & 0 & \sqrt{3}+3 & \sqrt{3} & -6 & 0 \\ -\sqrt{3} & -\sqrt{3} & 0 & -6 & \sqrt{3} & \sqrt{3}+3 & 0 & 0 \\ -\sqrt{3} & \sqrt{3} & 0 & 0 & -6 & 0 & \sqrt{3}+3 & -\sqrt{3} \\ \sqrt{3} & 2\alpha_2 & 0 & 0 & 0 & 0 & -\sqrt{3} & \alpha_2 \end{bmatrix} \quad (\text{A.9})$$

A.4 Application example

In order to apply the formulation of the framework method described above, two computer applications for the preprocessing, processing and postprocessing were developed. The preprocessing is performed by one application written in C[‡] language and works inside the *AutoCAD* (Autodesk, 2015) environment. The purpose of this program is to extract the geometric data of the mesh, drawn in an *AutoCAD* (Autodesk, 2015) file, and build the input file for the processing and postprocessing application. A *MATLAB* (MathWorks, 2013) routine is written so as to solve the mathematical problem, applying the formulation of the former section. Once the problem is solved, the application displays the results of strain energy and eigen-analysis.

The problem of the Timoshenko's column was selected (Timoshenko and Goodier, 1969) as the exact solution of it is known for a linear case. The geometry and restraints are shown in fig. A.2.

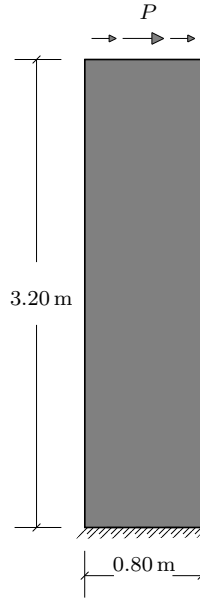


Figure A.2: Timoshenko's column geometry

For analyzing the column, a Young's module $E = 1,750$ MPa, a Poisson's ratio $\nu = 1/3$ and an applied load $P = 1,000$ N in the free end, as shown in fig. A.2, were considered. The load has a parabolic distribution. Five meshes were built, with 2, 4, 8 and 16 unit cells at the end where load is applied. The mesh with 4 unit cells in free end is shown in fig A.3. The shape of the each unit cell in this mesh corresponds to the one of fig. A.1b, in which the $A_2 = 0$ since $\nu = 1/3$.

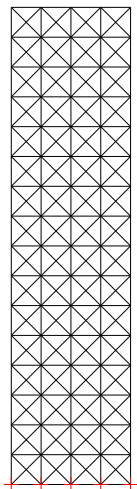


Figure A.3: Timoshenko's column mesh with 4 unit cells at the free end

The characteristic equation of the global stiffness matrix, $(\mathbf{K} - \lambda\mathbf{I})\Phi = \mathbf{0}$, was solved. In fig. A.4, three deformation modes of the framework mesh with 2 unit cells in the free end, are compared to the corresponding ones obtained with an analogous mesh of finite elements. Both problems were solved with the same mechanical properties of the material and same boundary conditions. In these graphical representations, same scale factor is used for comparison purposes.

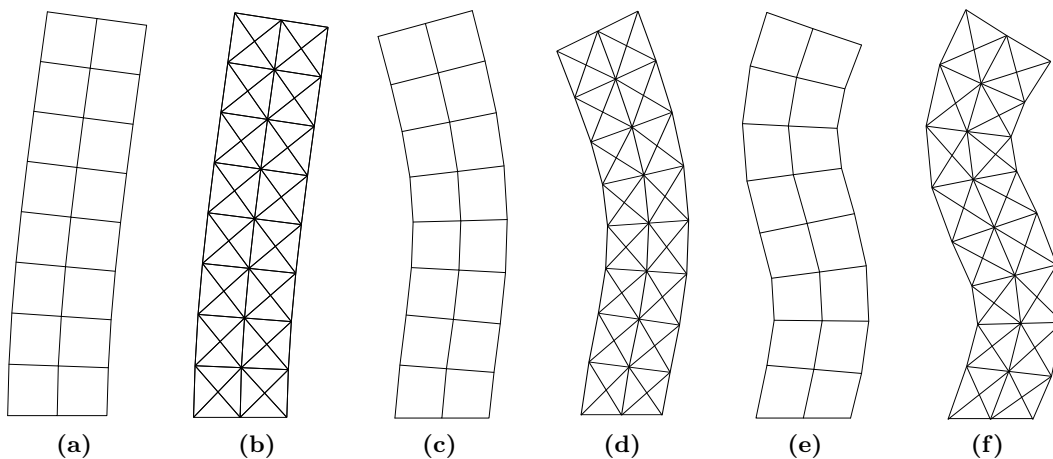


Figure A.4: Deformation modes 1(*a,b*), 2(*c,d*), and 3(*e,f*) of Timoshenko's column solved with: (*a,c,e*) finite element method and (*b,d,f*) framework method

In these figures, a similar configuration can be seen for all modes. The strain energy was also computed for all the meshes. In fig. A.5, the convergence to the real solution of strain energy for each mesh mentioned above can be observed. Several remarks can be placed from fig. A.5. An undesirable behaviour in convergence is observed, since although the solution is converging to a stationary value, this value does not correspond to the analytical solution of strain energy. The difference between these results is 2.25%. This phenomenon is quite similar to that presented in chapter 3, in which the rigid block models are studied.

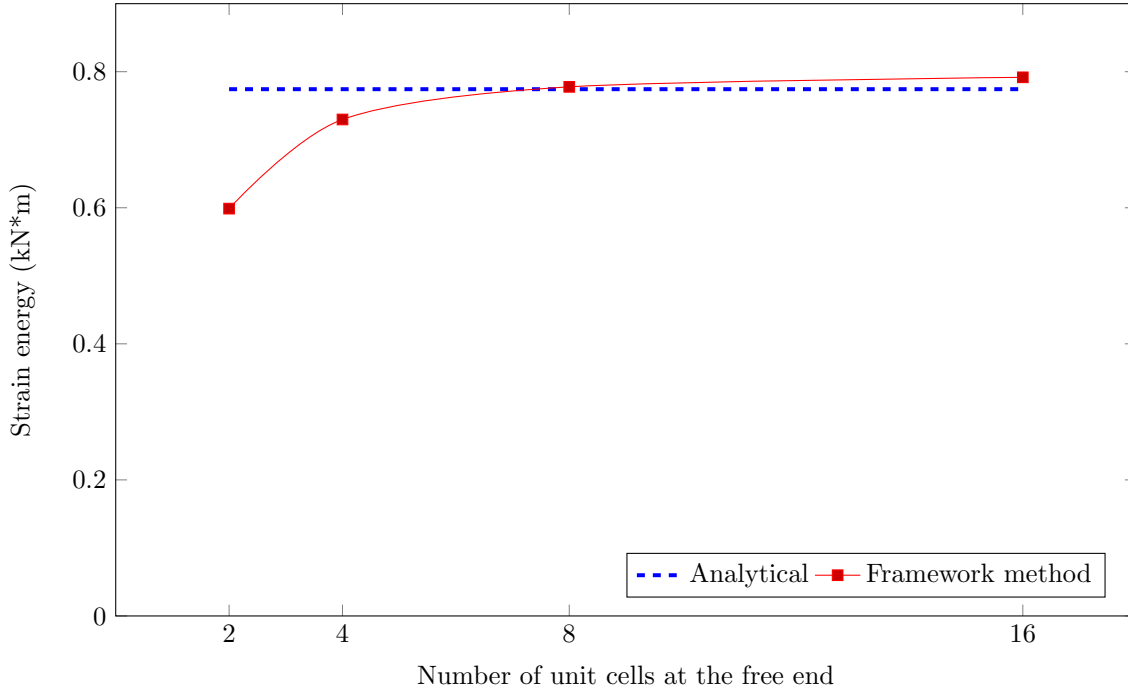


Figure A.5: Timoshenko's column convergence of the framework method to analytical solution in strain energy

In addition to the convergence issue, the method presents many other disadvantages. For instance that the unit-cell shape needs to be closer to a square, since the a dimension is fundamental for computing the area of the bars, which represents the mechanical behaviour of the material, a highly-distorted quadrilateral can not be solved with this method. For this reason, the method is not optimal for complex geometries. Nevertheless, new unit cells can be developed from the existing ones and applied to this type of problems.

In spite of this remarks, the framework method represents the origin of several numerical methods that are widely used. For example the idea of modeling a structure in an arrangement of simpler units, which their mechanical behaviour is easier to approximate, is used in strategies as the finite element method and rigid blocks models.

References

- Ambrosetti, C. (2000). *Sul comportamento sismico de un modulo strutturale di un monumento ad arco: Analisi numerica con modello ad attrito*. PhD thesis, Politecnico di Milano, Italia.
- Autodesk (2015). *Autodesk AutoCAD 2014 Student Version*. The Autodesk Inc.
- Belytschko, T. and Bachrach, W. E. (1986). Efficient implementation of the quadrilaterals with high coarse-mesh accuracy. *Computer Methods in Applied Mechanics and Engineering*, 54(3):279–301.
- Belytschko, T. and Bindeman, L. P. (1991). Assumed strain stabilization of the 4-node quadrilateral with 1-point quadrature for nonlinear problems. *Computer Methods in Applied Mechanics and Engineering*, 88(3):311–340.
- Belytschko, T., Liu, W. K., Moran, B., and Elkhodary, K. (2013). *Nonlinear Finite Elements for Continua and Structures*. John Wiley Sons, Ltd.
- Belytschko, T., ONG, J., LIU, W. K., and Kennedy, J. M. (1984). Hourglass control in linear and nonlinear problems. *Computer Methods in Applied Mechanics and Engineering*, 43(3):251–276.
- Bono, F., Tirelli, D., Verzelletti, G., Molina, G., and Renda, V. (1998). Shape memory alloy crossbracing of masonry walls: cyclic test of a large scale model and numerical analyses. *Workshop on Seismic Performance of Monuments*, pages 239–248.
- Cook, R. D. (1974). Improved two-dimensional finite element. *Journal of the Structural Division*, 100(9):1851–1863.
- Cook, R. D., Malkus, D. S., and Plesha, M. E. (1989). *Concepts and applications of finite element method*. John Wiley Sons, Ltd.
- Correia, J. R., Branco, F. A., and de Brito, J. (2007). Analysis of São Vicente de Fora church, Portugal. *Proceedings of the Institution of Civil Engineers-Structures and Buildings*, 160(4):187–196.
- De Borst, R., Crisfield, M. A., Remmers, J. J., and Verhoosel, C. V. (2012). *Nonlinear finite element analysis of solids and structures*. John Wiley Sons.

REFERENCES

- Dhanasekar, M., Kleeman, P. W., and Page, A. W. (1985). Biaxial stress-strain relations for brick masonry. *Journal of Structural Engineering-ASCE*, 111(5):1085–1100.
- Flanagan, D. P. and Belytschko, T. (1981). A uniform strain hexahedron and quadrilateral with orthogonal hourglass control. *International Journal for Numerical Methods in Engineering*, 17(5):679–706.
- García, N. (2012). Historic masonry buildings and tools for their structural study (in Spanish). *Iventio. La génesis de la cultura universitaria en Morelos*, 16:107–112.
- GDF (2004). Complementary technical standards of the Construction code for the Federal District (in Spanish). *Official Gazzete of the Federal District, México D.F.*
- Hrennikoff, A. (1949). Framework method and its technique for solving plane stress problems. *IABSE Publications*, 9:217–248.
- Hrennikoff, A. (1968). The finite element method in application to plane stress. *IABSE Publications*, pages 49–67.
- Irons, B., Ahmad, S., and Belytschko, T. (1980). Techniques of finite elements. *Journal of Applied Mechanics*, 47:978.
- Kosloff, D. and Frazier, G. A. (1978). Treatment of hourglass patterns in low order finite element codes. *International Journal for Numerical and Analytical Methods in Geomechanics*, 2(1):57–72.
- Kotronis, P., Mazars, J., and Davenne, L. (2003). The equivalent reinforced concrete model for simulating the behavior of walls under dynamic shear loading. *Engineering fracture mechanics*, 70(7):1085–1097.
- Maenchen, G. and Sack, S. (1964). The TENSOR code. *California. Univ., Livermore. Lawrence Radiation Lab.*, 3:181–210.
- MathWorks (2013). *MATLAB Version 8.1.0.604 (R2013a)*. The MathWorks Inc., Natick, Massachusetts.
- Meza, J. M., Orduña, A., and Ayala, A. G. (2008). Simplified procedure for the evaluation of seismic capacity of historic masonry buildings (in Spanish). *XVI Congreso Nacional de Ingeniería Estructural, SMIE México*.
- Nagtegaal, J. C., Parks, D. M., and Rice, J. (1974). On numerically accurate finite element solutions in the fully plastic range. *Computer methods in applied mechanics and engineering*, 4(2):153–177.
- Newmark, N. M. (1949). Numerical methods of analysis of bars, plates, and elastic bodies. *Numerical methods in Engineering*, pages 138–168.
- Orduña, A. (2003). *Seismic Assessment of Ancient Masonry Structures by Rigid Blocks Limit Analysis*. PhD thesis, Universidade do Minho, Portugal.

-
- Orduña, A., Anguiano, I., and Roeder, G. (2005). Use of numerical integration in the definition of yield functions for three-dimensional limit analysis of historical masonry buildings subjected to lateral loads (in Spanish). *XV Congreso Nacional de Ingeniería Sísmica, SMIS México*.
- Orduña, A. and Ayala, G. (2016*). Non-linear static analysis of rigid block models for structural assessment of ancient masonry constructions. *Under preparation*.
- Orduña, A., Peña, F., and Roeder, G. (2004a). State of the art on the structural analysis of historic masonry structures. Part I: mechanical behaviour and constitutive models (in Spanish). *XIV Congreso Nacional de Ingeniería Sísmica, SMIS México*.
- Orduña, A., Peña, F., and Roeder, G. (2004b). State of the art on the structural analysis of historic masonry structures. Part II: models of analysis (in Spanish). *XIV Congreso Nacional de Ingeniería Sísmica, SMIS México*.
- Orduña, A., Roeder, G., and Peña, F. (2007). Seismic assessment of historical masonry constructions: comparison of three models of analysis (in Spanish). *Revista de Ingeniería Sísmica, SMIS México*, 77:71–88.
- Pegon, P., Pinto, V. P., and Gérardin, M. (2001). Numerical modeling of stone-block monumental structures. *Computers and Structures*, 79(22):2165–2181.
- Simo, J. and Taylor, R. (1986). A return mapping algorithm for plane stress elastoplasticity. *International Journal for Numerical Methods in Engineering*, 22(3):649–670.
- Taylor, R. L. (2014). *FEAP, A Finite Element Analysis Program, Programmers Manual*. Department of Civil and Environmental Engineering, University of California at Berkeley.
- Timoshenko, S. and Goodier, J. (1969). *Theory of elasticity*. McGraw-Hill.
- Wilkins, M. L., Blum, R. E., Cronshagen, E., and Grantham, P. (1975). *A method for computer simulation of problems in solid mechanics and gas dynamics in three dimensions and time*. Lawrence Livermore Laboratory.
- Wilson, E. L., Taylor, R. L., Doherty, W. P., and Ghaboussi, J. (1973). Incompatible displacement models. *Numerical and computer methods in structural mechanics*, 43.
- Zienkiewicz, O. C. and Taylor, R. L. (2000). *The finite element method. Volume 1: The basis*. Butterworth-heinemann.